Beneficial Effects of Exendin-4 on Experimental Polyneuropathy in Diabetic Mice

Tatsuhito Himeno,[1] Hideki Kamiya,[1,2] Keiko Naruse,[3] Norio Harada,[4] Nobuaki Ozaki,[1] Yusuke Seino,[1] Taiga Shibata,[1] Masaki Kondo,[1] Jiro Kato,[1] Tetsuji Okawa,[1] Ayako Fukami,[1] Yoji Hamada,[5] Nobuya Inagaki,[4] Yutaka Seino,[6] Daniel J. Drucker,[7] Yutaka Oiso,[1] and Jiro Nakamura[1]

OBJECTIVE—The therapeutic potential of exendin-4, an agonist of the glucagon-like peptide-1 receptor (GLP-1R), on diabetic polyneuropathy (DPN) in streptozotocin (STZ)-induced diabetic mice was investigated.

RESEARCH DESIGN AND METHODS—The presence of the GLP-1R in lumbar dorsal root ganglion (DRG) was evaluated by immunohistochemical analyses. DRG neurons were dissected from C57BL6/J mice and cultured with or without Schwann cell–conditioned media in the presence or absence of GLP-1 (7–37) or exendin-4. Then neurite outgrowth was determined. In animal-model experiments, mice were made diabetic by STZ administration, and after 12 weeks of diabetes, exendin-4 (10 nmol/kg) was intraperitoneally administered once daily for 4 weeks. Peripheral nerve function was determined by the current perception threshold and motor and sensory nerve conduction velocity (MNCV and SNCV, respectively). Sciatic nerve blood flow (SNBF) and intraepidermal nerve fiber densities (IENFDs) also were evaluated.

RESULTS—The expression of the GLP-1R in DRG neurons was confirmed. GLP-1 (7–37) and exendin-4 significantly promoted neurite outgrowth of DRG neurons. Both GLP-1R agonists accelerated the impaired neurite outgrowth of DRG neurons cultured with Schwann cell–conditioned media that mimicked the diabetic condition. At the doses used, exendin-4 had no effect on blood glucose or HbA_{1c} levels. Hypoalgesia and delayed MNCV and SNCV in diabetic mice were improved by exendin-4 without affecting the reduced SNBF. The decreased IENFDs in sole skins of diabetic mice were ameliorated by exendin-4.

CONCLUSIONS—Our findings indicate that exendin-4 ameliorates the severity of DPN, which may be achieved by its direct actions on DRG neurons and their axons. ***Diabetes* 60:2397–2406, 2011**

From the [1]Department of Endocrinology and Diabetes, Nagoya University Graduate School of Medicine, Nagoya, Japan; the [2]Department of Chronic Kidney Disease Initiatives, Nagoya University Graduate School of Medicine, Nagoya, Japan; the [3]Department of Internal Medicine, School of Dentistry, Aichi-Gakuin University, Nagoya, Japan; the [4]Department of Diabetes and Clinical Nutrition, Graduate School of Medicine, Kyoto University, Kyoto, Japan; the [5]Department of Metabolic Medicine, Nagoya University Graduate School of Medicine, Nagoya, Japan; the [6]Division of Diabetes, Clinical Nutrition, and Endocrinology, Department of Medicine, Kansai Electric Power Hospital, Osaka, Japan; and the [7]Department of Medicine, Mt. Sinai Hospital, Samuel Lunenfeld Research Institute, University of Toronto, Toronto, Ontario, Canada.

Corresponding author: Hideki Kamiya, hkamiya@med.nagoya-u.ac.jp.

Received 19 October 2010 and accepted 30 June 2011.

DOI: 10.2337/db10-1462

This article contains Supplementary Data online at http://diabetes.diabetesjournals.org/lookup/suppl/doi:10.2337/db10-1462/-/DC1.

Diabetes is the most common cause of peripheral neuropathy encompassing both mononeuropathy and polyneuropathy (1,2). In general, diabetic polyneuropathy (DPN) develops symmetrically in a nerve length–dependent fashion, with dying-back degeneration of both myelinated and unmyelinated fibers. Diabetic patients may exhibit various symptoms of DPN, such as spontaneous pain, hyperalgesia, and diminished sensation (3). It has been shown that tight glycemic control is effective in slowing the progression of DPN but cannot completely prevent it (4). We have focused on the role of reduced nerve blood flow in the development and the progression of DPN (5–7). In addition to the hemodynamic deterioration of diabetic nerves, previous studies have described a number of pathogenic mechanisms suggesting favorable treatments of DPN, but these treatments have generally failed in clinical trials (2). Thus, at this time, there are few effective therapies for DPN. Because the etiology of DPN seems to be multifactorial, a multitargeted intervention may be necessary.

An incretin hormone, glucagon-like peptide (GLP)-1, is released from the L cells of the small intestine (8). GLP-1 and a GLP-1 receptor (GLP-1R) agonist, exendin-4, potentiate glucose-stimulated insulin secretion after a meal, and GLP-1R agonists have been used as therapeutic agents for type 2 diabetes (9–11). In addition to this antihyperglycemic effect, GLP-1R agonists have been shown to have several actions, such as slowing gastric emptying (11) and reducing food intake (12), that are independent of insulin secretion (13). Many reports have suggested that GLP-1R agonists have neurotrophic and neuroprotective properties in some neurons and neural cells (14–18). It has been revealed that prolonged neurite extension is induced by mechanisms involving cAMP (19), which also is involved in the cascade mechanisms of insulin secretion induced by GLP-1R agonists. In addition, the therapeutic effects of GLP-1R agonists on stroke, Parkinsonism, and pyridoxine-induced peripheral sensory neuropathy (18–20) using animal models have been reported.

Although several beneficial effects of GLP-1 or the GLP-1R agonist on central and peripheral nervous systems have been reported, their effects under the diabetic condition have not yet been evaluated. Here, we investigated the effects of the GLP-1R agonist exendin-4 on DPN by both in vitro and in vivo experiments.

RESEARCH DESIGN AND METHODS

Schwann cell culture and preparation of Schwann cell–conditioned media. Immortalized Schwann cells (IMS32), established by long-term culture of adult mouse dorsal root ganglions (DRGs) and peripheral nerves (21), were a gift from Dr. Kazuhiro Watabe. IMS32 were cultured in Dulbecco's

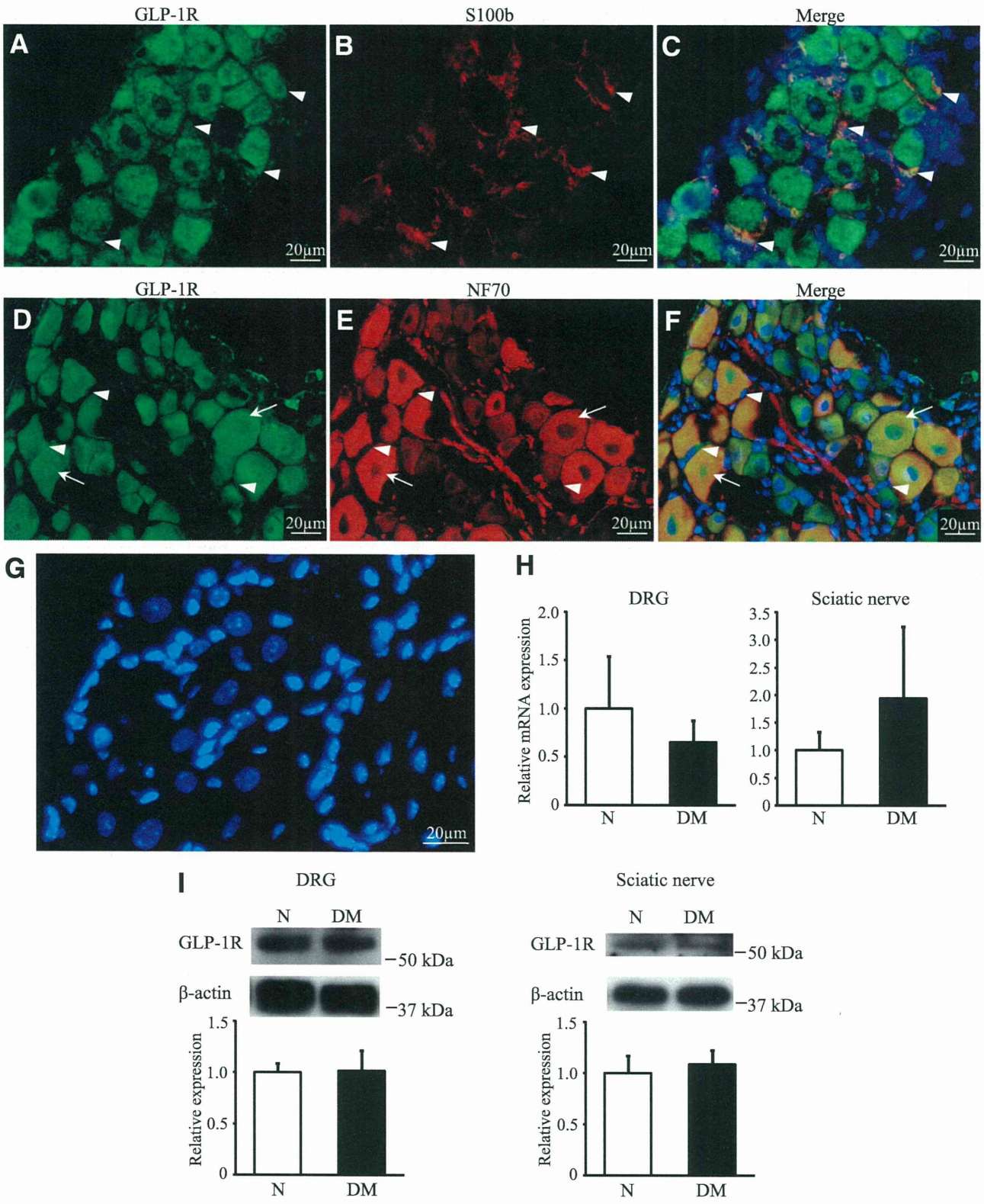

FIG. 1. Expression of GLP-1R in DRGs and sciatic nerves. *A*, *C*, *D*, and *F*: Immunohistochemically, GLP-1R (green) in DRG was detected with anti–GLP-1R antibody (sc-66911). Both DRG neurons, indicated by NF70 antibody (red) (*E* and *F*), and satellite glia cells, indicated by S100b antibody (red) (*B* and *C*), expressed GLP-1R. *C*, *F*, and *G*: Nuclei (blue) were stained with diaminido phenyl indol. *A–F*: White arrowheads indicate satellite glia cells. White arrows indicate neurons. *G*: GLP-1R protein (red) was not detected in DRG neurons of *glp1r*$^{-/-}$ mice. *H*: The transcript levels of *glp1r* in DRGs and sciatic nerves of diabetic mice were not significantly different from those of normal mice (DRG: normal mice [N] [n = 6], 1 ± 0.54, threshold cycle value [C_t] of *glp1r* 34.8 ± 2.3, C_t of 18S rRNA 11.2 ± 1.0 and diabetic mice [DM] [n = 7], 0.65 ± 0.23, C_t of *glp1r* 34.0 ± 1.5, C_t of 18S rRNA 11.0 ± 1.4, P = 0.544; sciatic nerves: normal mice [n = 4], 1 ± 0.34, C_t of *glp1r* 33.6 ± 1.6, C_t of 18S rRNA 14.7 ± 1.1 and diabetic mice [n = 5], 1.95 ± 1.29, C_t of *glp1r* 34.5 ± 1.3, C_t of 18S rRNA 12.5 ± 2.8, P = 0.606). *I*: There were no significant differences in the protein levels of GLP-1R

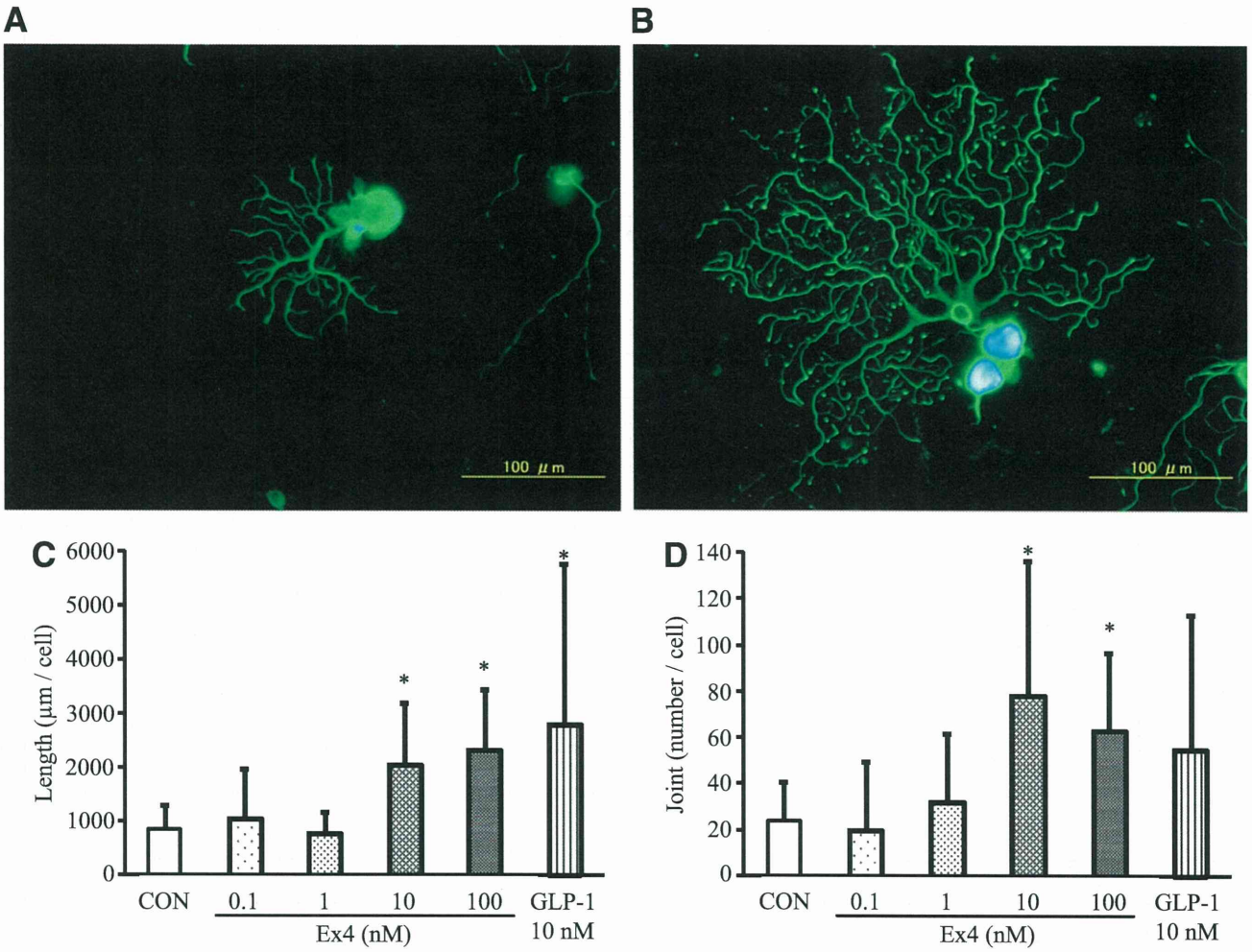

FIG. 2. Neurite outgrowth of DRG neurons by GLP-1 (7–37) and exendin-4 (Ex4). Representative fluorescence micrograph of DRG neurons cultured in the absence (*A*) or presence (*B*) of GLP-1 (7–37) (GLP-1) (10 nmol/L). GLP-1 (7–37) (10 nmol/L) or exendin-4 (0.1, 1, 10, and 100 nmol/L) increased the total neurite length (*C*) and joint number (*D*) of neurites. Results are means ± SD. CON, control medium. **P* < 0.05 vs. control medium (*n* = 10–20). Control medium, joint number 23.5 ± 17.2 per cell, total length 833 ± 462 μm per cell, 10 nmol/L GLP-1 (7–37); joint number 54.8 ± 58.3, total length 2,786 ± 2,976, 0.1 nmol/L exendin-4; joint number 19.81 ± 29.59, total length 1,056.3 ± 904.5, 1 nmol/L exendin-4; joint number 32.23 ± 29.35, total length 761.9 ± 414.7, 10 nmol/L exendin-4; joint number 78.1 ± 58.4, total length 2,035 ± 1,162, 100 nmol/L exendin-4; and joint number 63.1 ± 33.8, total length 2,329 ± 1,104. (A high-quality digital representation of this figure is available in the online issue.)

modified Eagle's medium (DMEM) (Sigma-Aldrich, St. Louis, MO) containing 5.5 mmol/L D-glucose, penicillin (100 units/mL)-streptomycin (100 mg/mL), and 5% FBS (Moregate Biotech, Bulimba QLD, Australia). When the cells reached ~70% confluency, they were maintained in DMEM with 2% FBS containing 5.5 mmol/L D-glucose (normal glucose [NG]) or 30 mmol/L D-glucose (high glucose [HG]). After a 3-day culture, the cells were maintained in serum-free DMEM containing NG or HG. After 24 h, culture media were collected, concentrated 10 times using 10 kD centrifugal filters (Amicom Ultra-15; Nihon Millipore, Tokyo, Japan), and frozen at −80°C until use. We defined these media as NG-IMS media or HG-IMS media.

Primary culture of DRG neurons and evaluation of neurite outgrowth. DRG neuron cultures were prepared from 5-week-old male C57BL/6 mice (Chubu Kagaku Shizai, Nagoya, Japan), as previously described (22). In brief, DRGs were collected, dissociated by collagenase (Wako Pure Chemical, Osaka, Japan), and diluted in a medium consisting of F-12 media, 10 mmol/L glucose, and 30 nmol/L selenium. Isolated DRG neurons were seeded on glass coverslips coated with poly-L-lysine. DRG neurons were cultured with or without 10 nmol/L GLP-1 (7–37) (Bachem Bioscience, Torrance, CA) or exendin-4 (Sigma-Aldrich) (0.1, 1, 10, and 100 nmol/L). To evaluate the effects of GLP-1R agonists on impaired neurite outgrowth under the diabetic condition, DRG neurons were cultured in HG-IMS media that was diluted one-tenth with F-12 media.

After a 24-h culture, DRG neurons fixed with 4% paraformaldehyde were immunostained with rabbit polyclonal antineurofilament heavy-chain antibody (1:5,000; Nihon Millipore) and visualized with Alexa Fluor 488–coupled goat anti-rabbit IgG antibody (1:200; Invitrogen, Carlsbad, CA). Coverslips were counterstained with 4′,6-Diamidine-2′-phenylindole dihydrochloride (Merck, Tokyo, Japan). Images were captured by a charge-coupled device camera (DP70; Olympus Optical, Tokyo, Japan) using a fluorescence microscope (BX51; Olympus Optical). Neurite outgrowth was observed in 10–20 neurons per coverslip and evaluated by a computed image analysis system (Angiogenesis Image Analyzer version 2; KURABO Industries, Osaka, Japan).

Animals and induction of diabetes. Five-week-old male C57BL/6 mice (Chubu Kagaku Shizai) were used. Diabetes was induced by intraperitoneal injection of streptozotocin (STZ) (150 mg/kg; Sigma-Aldrich). Control mice received an equal volume of citric acid buffer. One week after STZ administration,

evaluated by Western blotting analyses between diabetic and normal mice (DRG: normal mice [*n* = 4], 1 ± 0.09 and diabetic mice [*n* = 4], 1.02 ± 0.20, *P* = 0.875; sciatic nerves: normal mice [*n* = 4], 1 ± 0.17 and diabetic mice [*n* = 4], 1.09 ± 1.35, *P* = 0.438). (A high-quality digital representation of this figure is available in the online issue.)

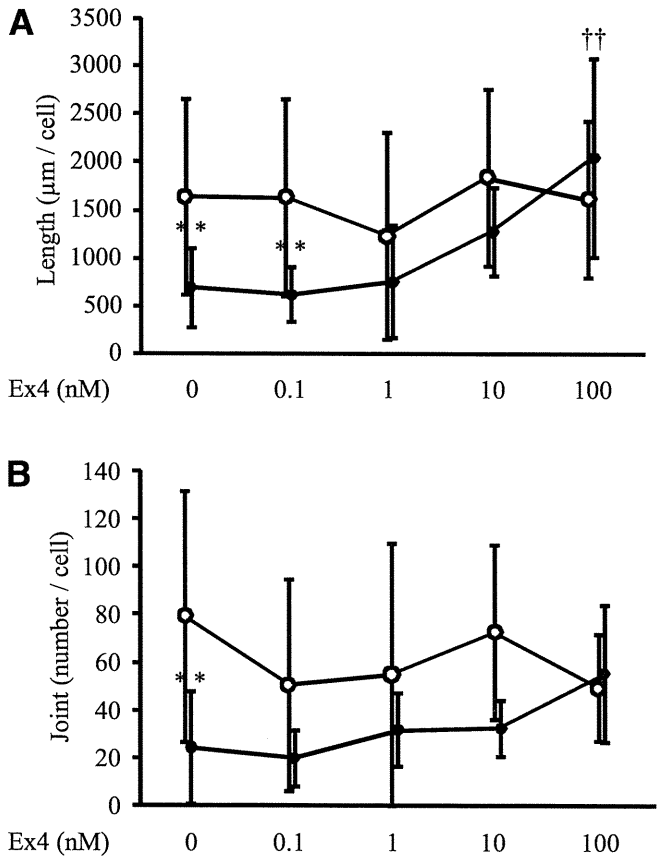

FIG. 3. Neurite outgrowth of DRG neurons in IMS media with or without exendin-4 (Ex4). Total length (*A*) and joint number (*B*) of DRG neurons cultured in IMS media were measured. Decreased total length and joint number of DRG neurites cultured in HG were ameliorated by Ex4 in a dose-dependent fashion. Results are means ± SD. ●, Neurite cultured in HG-IMS media; ○, neurite cultured in NG-IMS media. NG-IMS media were obtained from IMS cultured in F-12 media with 5.5 mmol/L D-glucose; HG-IMS media were obtained from IMS cultured in F-12 media with 30 mmol/L D-glucose. **P < 0.005 vs. NG-IMS media without exendin-4; ††P < 0.005 vs. HG-IMS media without exendin-4. n = 10–20. Total length: NG 1,635 ± 1,014 μm per cell and HG 684 ± 410; joint number: NG 79.2 ± 52.5 per cell and HG 24.2 ± 23.8. Total length: HG with 10 nmol/L exendin-4 1,278 ± 457 and HG with 100 nmol/L exendin-4 2,045 ± 1,029. Joint number: HG with 10 nmol/L exendin-4 32.3 ± 12.0 and HG with 100 nmol/L exendin-4 55.1 ± 28.8. Total length: NG with 10 nmol/L exendin-4 1,839 ± 915 and NG with 100 nmol/L exendin-4 1,614 ± 821. Joint number: NG with 10 nmol/L exendin-4 72.7 ± 36.3 and NG with 100 nmol/L exendin-4 49.3 ± 22.3.

the mice with plasma glucose concentrations >16 mmol/L were selected as diabetic mice. Twelve weeks after the induction of diabetes, mice were treated once daily with exendin-4 (10 nmol/kg in 0.1 mL of water i.p.) or vehicle (saline) over 4 weeks (n = 10 in each group). Before and after exendin-4 treatment, fasting blood glucose levels and HbA_{1c} were examined by a FreeStyle Freedom Glucose Meter (Nipro, Osaka, Japan) and a RAPIDIA Auto HbA1c-L assay kit using latex agglutination (Fujirebio, Tokyo, Japan), respectively. After the exendin-4 treatment, intraperitoneal glucose tolerance tests (IPGTTs) were performed on the mice. Serum insulin and glucagon levels also were measured in fasted mice by an insulin ELISA kit (Morinaga Institute of Biological Science, Yokohama, Japan) and a glucagon enzyme immune assay kit (Yanaihara Institute, Fujinomiya, Japan), respectively. The Nagoya University Institutional Animal Care and Use Committee approved the protocols of this experiment.

Measurement of current perception threshold using a neurometer. To determine a nociceptive threshold, the current perception threshold (CPT) was measured in 12- and 16-week diabetic and age-matched normal mice using a CPT/laboratory neurometer (Neurotron, Denver, CO). The electrodes (SRE-0405–8; Neurotron) for stimulation were attached to plantar surfaces. Each mouse was kept in a Ballman cage (Natsume Seisakusho, Tokyo, Japan) suitable for light restraint to keep awake. Three transcutaneous-sine-wave stimuli with different frequencies (2,000, 250, and 5 Hz) were applied to the plantar surfaces. The intensity of each stimulation was gradually increased automatically (increments of 0.01 mA for 5 and 250 Hz and increments of 0.02 mA for 2,000 Hz). The minimum intensity at which the mouse withdrew its paw was defined as the CPT. Six consecutive measurements were conducted at each frequency.

Nerve conduction velocity. Mice anesthetized with pentobarbital were placed on a heated pad in a room maintained at 25°C to ensure a constant rectal temperature of 37°C. Motor nerve conduction velocity (MNCV) was determined between the sciatic notch and ankle with a Neuropak NEM-3102 instrument (Nihon-Koden, Osaka, Japan), as previously described (5,6,23). The sensory nerve conduction velocity (SNCV) was measured between the knee and ankle with retrograde stimulation.

Sciatic nerve blood flow. Sciatic nerve blood flow (SNBF) was measured by laser-Doppler flowmetry (FLO-N1; Omegawave, Tokyo, Japan). The thigh skin of an anesthetized mouse was cut along the femur and then an incision through the fascia was carefully made to expose the sciatic nerve. Five minutes after this procedure, the blood flow was measured by a laser-Doppler probe placed 1 mm above the nerve. During this measurement, the mouse was placed on a heated pad in a room maintained at 25°C to ensure a constant rectal temperature of 37°C.

Tissue collection. Four weeks after the treatment with exendin-4, mice were killed by an overdose of pentobarbital or perfusion with 50 mL of 4% paraformaldehyde. DRGs and sciatic nerves were obtained from normal and diabetic mice. Some of the tissues were snap frozen in liquid nitrogen, followed by preservation at –80°C until use, and others were transferred to RNAlater solution (Invitrogen), followed by freezing preservation for RT-PCR. For immunohistochemistry, DRGs, pancreas, and sole skin were excised, fixed in 4% paraformaldehyde, and frozen in optimal cutting temperature compound (Sakura Finetechnical, Tokyo, Japan) after cryoprotection.

GLP-1R mRNA expression in DRGs and sciatic nerves. RNAs were extracted from frozen samples of DRGs and sciatic nerves using Isogen (Nippon Gene, Toyama, Japan) and were quantified spectrophotometrically. Starting from 1 μg of RNA, cDNA was synthesized using ReverTra Ace (Toyobo, Osaka, Japan). TaqMan gene expression assays (Applied Biosystems, Foster City, CA) were used for GLP-1R and 18S rRNA for the endogenous control. Real-time quantitative RT-PCR was performed using the Mx3000P QPCR System (Stratagene, La Jolla, CA). Relative quantity was calculated by the $\Delta\Delta C_t$ method with normalization to 18S rRNA (24).

Western blotting. DRGs and sciatic nerves were used for Western blotting. Samples were lysed in detergent lysis buffer (Cell Lysis Buffer; Cell Signaling Technology, Boston, MA) adding 1 mmol/L phenylmethanesulfonylfluoride (Sigma-Aldrich), following centrifugation. Proteins were quantitated the concentrations with a bicinchoninic acid assay (Sigma Chemical) and were transferred to polyvinylidene fluoride membranes (Millipore, Billerica, MA) after SDS-PAGE. Membranes were blocked and incubated with rabbit polyclonal anti–GLP-1R antibody (1:100; Santa Cruz Biotechnology, Santa Cruz, CA) and rabbit polyclonal anti–β-actin antibody (1:10,000; Abcam, Cambridge, MA). Antigen detection was performed using ECL Plus Western Blotting Detection Reagents (Amersham Pharmacia Biotech, Piscataway, NJ) with horseradish peroxidase–conjugated anti-rabbit IgG antibody (1:6,000; Cell Signaling Technology). Images were scanned and their densities were determined by ImageJ (National Institutes of Health, Bethesda, MD). The expression of the GLP-1R protein was corrected by β-actin density, and the expression in tissues of normal mice was arbitrarily set at 1.0.

Immunocytochemistry and frozen section staining. After a 24-h culture, DRG cells, as indicated above, were fixed with 4% paraformaldehyde. The cells were blocked with 3% goat serum, and the following primary antibodies were applied to the glass coverslips at 4°C overnight: rabbit polyclonal anti–GLP-1R antibody (1:200, sc-66911; Santa Cruz Biotechnology); mouse monoclonal anti-neurofilament 70 kDa (NF70) antibody (1:1,000, MAB1615; Millipore); and mouse monoclonal anti-S100b antibody (1:300, S2532; Sigma-Aldrich). After washing, the following secondary antibodies were loaded for 1 h at room temperature in a dark box: Alexa Fluor 488–coupled goat anti-rabbit IgG antibody (1:200; Invitrogen) and Alexa Fluor 594–coupled goat anti-mouse antibody (1:300; Invitrogen).

For immunohistochemistry, after the microwave irradiation in citrate buffer (pH 6.0), cryostat sections were blocked with 5% skim milk (Meiji Milk, Tokyo, Japan) and the following primary antibodies were applied to the sections at 4°C overnight: rabbit polyclonal anti–protein-gene-product 9.5 (PGP 9.5) antibody (1:500; Millipore); guinea-pig polyclonal anti-insulin antibody (1:500, Ab7842-500; Abcam); rabbit polyclonal anti–GLP-1R antibody (1:200, sc-66911, Santa Cruz Biotechnology; LS-A1205 and LS-A1206, MBL International, Woburn, MA); mouse monoclonal NF70 antibody (1:1,000; Millipore); and mouse monoclonal anti-S100b antibody (1:300; Sigma-Aldrich). After washing, the secondary antibodies, as indicated above, were loaded for 1 h at room temperature.

TABLE 1
Body weight, blood glucose, and HbA_{1c} levels in normal and diabetic mice

	Normal mice			Diabetic mice		
		Posttreatment			Posttreatment	
	Pretreatment	Saline	Exendin-4	Pretreatment	Saline	Exendin-4
n	8	5	6–8	9–10	8	9
Blood glucose (mmol/L)	9.1 ± 1.6	9.1 ± 1.6	8.7 ± 2.4	23.1 ± 2.8*	26.6 ± 2.9*	23.9 ± 2.3*
HbA_{1c} (%)	4.0 ± 0.1	4.1 ± 0.2	3.9 ± 0.1	7.6 ± 1.2*	7.7 ± 2.1*	6.9 ± 2.1*
Body weight (g)	31 ± 3	31 ± 3	27 ± 2†	26 ± 3*	24 ± 4*	23 ± 2*

Data are means ± SD. *$P < 0.05$ vs. pretreatment normal mice. †$P < 0.05$ vs. normal mice treated with saline.

Coverslips and tissues were counterstained with diaminido phenyl indol (Merck). Images were captured by a charge-coupled device camera (DP70; Olympus Optical) using a fluorescence microscope (BX51; Olympus Optical).

Measurement of intraepidermal nerve fiber densities. Nerve fibers stained with anti–PGP 9.5 antibody were counted as previously reported (25). In brief, each individual nerve fiber with branching inside the epidermis was counted as one, and a nerve fiber with branching in the dermis was counted separately. Six fields from each section were randomly selected for the intraepidermal nerve fiber (IENF) densities (IENFDs). IENFDs were derived and expressed as epidermal nerve fiber numbers per length of the epidermal basement membrane (fibers per millimeter).

Statistical analysis. All the group values were expressed as means ± SD. Statistical analyses were made by one-way ANOVA, with the Bonferroni correction for multiple comparisons. All analyses were performed by personnel who were unaware of the animal identities.

RESULTS

DRG neurons and satellite cells expressed GLP-1Rs. To confirm the quality of GLP-1R antibody, we stained the islets of *glp1r*$^{-/-}$ mice. GLP-1R antibody obtained from Santa Cruz (sc-66911) detected the β-cells of wild-type mice but not those of *glp1r*$^{-/-}$ mice. In contrast, GLP-1R antibodies from MBL International (LS-A1205 and LS-A1206) nonspecifically stained the islets of *glp1r*$^{-/-}$ mice (Supplementary Fig. 1). In addition to immunohistochemistry, GLP-1R protein in the pancreas of wild-type mice was specifically detected and that of *glp1r*$^{-/-}$ mice was undetected with the GLP-1R antibody from Santa Cruz by Western blotting methods (Supplementary Fig. 2). Therefore, in this study, we used sc-66911 as a primary antibody to detect the expression of GLP-1R in DRGs. GLP-1R expression was detected in both DRG neurons indicated by NF70 and satellite cells indicated by S100b antibody (Fig. 1*A–F*). In contrast to these wild-type mice DRGs, GLP-1R expression was not detected in the DRGs of *glp1r*$^{-/-}$ mice (Fig. 1*G*). To further evaluate the localization of GLP-1R, we stained enzymatically dissociated DRG cells with GLP-1R antibody in addition to S100b or NF70 antibody. GLP-1R proteins also were expressed in both DRG neurons and satellite cells by this immucytochemical method (Supplementary Fig. 3).

GLP-1R agonists promoted neurite outgrowth of DRG neurons. In our DRG culture system, GLP-1R protein was expressed in all neurons and in about two-thirds of glia cells (data not shown). Therefore, we used our DRG culture system to evaluate the impact of the GLP-1R agonist on the sensory nervous system, especially sensory neurons.

Neurite outgrowth of DRG neurons was increased in the presence of GLP-1 (7–37) or exendin-4 (Fig. 2*A* and *B*). Total length and joint number of neurites were significantly increased by GLP-1 (7–37) or exendin-4 (joint number: control vs. 10 nmol/L exendin-4, $P = 0.0002$; control vs. 100 nmol/L exendin-4, $P = 0.0093$; and control vs. 10 nmol/L GLP-1 (7–37), $P < 0.0001$; total length: control vs. 10 nmol/L exendin-4, $P = 0.0003$; control vs. 100 nmol/L exendin-4, $P < 0.0001$; and control vs. 10 nmol/L GLP-1 (7–37), $P < 0.0001$) (Fig. 2*C* and *D*).

Exendin-4 ameliorated high glucose–induced reduction in neurite outgrowth of DRG neurons. DRG neurons cultured with HG-IMS media, which mimicked the diabetic state, had shorter neurites and smaller joint numbers compared with those cultured with NG-IMS media, which mimicked the nondiabetic normal state (total length: $P = 0.0205$, joint number: $P = 0.0006$) (Fig. 3). The impaired neurite outgrowth of DRG neurons cultured with HG-IMS media was improved by exendin-4 (total length: HG with 10 nmol/L exendin-4, $P = 0.1620$, and HG with 100 nmol/L exendin-4, $P = 0.0012$; joint number: HG with 10 nmol/L exendin-4, $P = 0.5871$, and HG with 100 nmol/L exendin-4, $P = 0.0433$). In contrast, exendin-4 did not promote the neurite outgrowth of DRG neurons cultured with NG-IMS media.

Levels of GLP-1R in DRGs and sciatic nerves were not impaired in diabetic mice. To ascertain the levels of *glp1r* mRNA and protein, we carried out real-time PCR analyses and Western blotting analyses in the DRGs and sciatic nerves of normal and diabetic mice before the exendin-4 treatment. The levels of *glp1r* transcript in DRGs and sciatic nerves of diabetic mice were not significantly different between those of normal mice (DRG: $P = 0.544$, sciatic nerves: $P = 0.606$) (Fig. 1*H*). Furthermore, there were no significant differences in GLP-1R protein contents between diabetic and normal mice (DRG: $P = 0.875$, sciatic nerves: $P = 0.438$) (Fig. 1*I*).

Body weights, blood glucose levels, and HbA_{1c}. At 12 weeks, diabetic mice showed severe hyperglycemia ($P = 0.0003$) and significantly reduced body weight gain ($P = 0.003$). Random blood glucose levels measured during the experimental period were not significantly different in any group. Exendin-4 treatment for 4 weeks did not alter body weight, blood glucose, or HbA_{1c} levels in the diabetic groups (Table 1).

Serum insulin and glucagon levels and IPGTTs. After the exendin-4 treatment, serum insulin levels were significantly decreased in diabetic mice, and exendin-4 administration provided no significant improvement in both diabetic and normal mice (Supplementary Fig. 4*A*). In IPGTT, blood glucose levels in diabetic mice after 15 min of glucose injection were significantly elevated compared with those in normal mice. These elevations were not significantly decreased by exendin-4 treatment (Supplementary Fig. 4*C*).

Although serum glucagon concentrations were not incremented in diabetic mice compared with those in normal mice, the concentrations in diabetic mice had a high propensity to be decreased by exendin-4 treatment (Supplementary Fig. 4*B*).

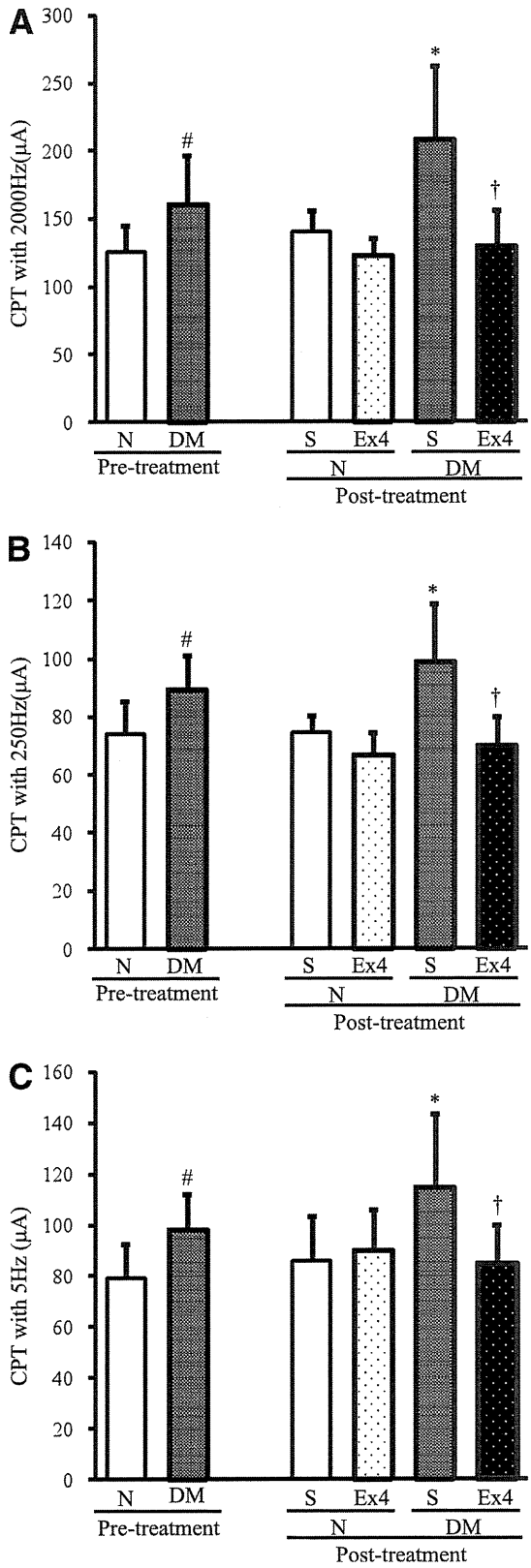

FIG. 4. Evaluation of sensory nerve functions. Measurements of CPTs at 2,000 (*A*), 250 (*B*), and 5 (*C*) Hz by a neurometer were performed before and at the end of exendin-4 (Ex4) administration. CPTs for all pulses were significantly increased in the diabetic group (DM), and these deficits were significantly prevented by exendin-4. N, normal mice; S, saline. Results are means ± SD. #P < 0.05 vs. pretreatment normal mice; *P < 0.05 vs. saline-treated normal mice; †P < 0.05 vs. saline-treated diabetic mice. Saline-treated normal mice, n = 8; exendin-4–treated normal mice, n = 8; saline-treated diabetic mice, n = 9; exendin-4–treated diabetic mice, n = 9.

Reduced sensory perception in diabetic mice was ameliorated by exendin-4 administration. After 12 weeks of diabetes, CPTs at 5, 250, and 2,000 Hz were significantly increased compared with those in normal mice (5 Hz: P = 0.015, 250 Hz: P = 0.019, and 2,000 Hz: P = 0.028), representing hypoalgesia in diabetic mice. After the 4 weeks of exendin-4 administration, these deficits in sensation were significantly improved in diabetic mice compared with saline-treated diabetic controls (5 Hz: P = 0.0161, 250 Hz: P = 0.0012, and 2,000 Hz: P = 0.0011). The injection of exendin-4 into normal mice did not induce significant changes in CPTs (Fig. 4*A–C*).

Exendin-4 improved delayed NCVs in diabetic mice. MNCVs and SNCVs of diabetic mice were significantly delayed compared with those of normal mice (MNCV: P = 0.0341, SNCV: P = 0.0489). The delay in MNCVs and SNCVs was significantly restored by exendin-4 treatment (MNCV: P = 0.0289, SNCV: P = 0.0201) (Fig. 5*A* and *B*). However, exendin-4 administration did not alter NCVs in normal mice.

Nerve fibers in epidermis were preserved by exendin-4. IENFDs were evident in both the epidermis and the dermis of the foot skin by the fluorescent imaging (Fig. 6*A*). Although IENFDs were decreased in diabetic mice (P = 0.0011), this decrement was significantly ameliorated by exendin-4 (P = 0.0007) (Fig. 6*B*). Administration of exendin-4 did not change IENFDs in normal mice (P = 0.2212).

Exendin-4 had no effects on SNBF. SNBF in diabetic mice was significantly decreased compared with those in normal mice (P = 0.0203), and the decrease was not ameliorated by exendin-4 (P = 0.7407) (Fig. 7).

DISCUSSION

In this study, we investigated whether GLP-1R agonists have therapeutic effects on DPN. First, we confirmed the expression of the GLP-1R on DRG neurons by immunohistochemical analyses. Second, we observed that both GLP-1 (7–37) and exendin-4 promoted neurite outgrowth of DRG neurons, and exendin-4 ameliorated the impaired neurite outgrowth of DRG neurons in conditioned media obtained from Schwann cell cultures under high-glucose conditions. We then demonstrated that administration of exendin-4 improved the reduced sensory perception of the plantar pedis, delayed NCVs of hindlimbs, and decreased IENFDs of the plantar skin in diabetic mice. However, neither the hyperglycemic state nor decreased SNBF were improved by exendin-4. These results indicate that exendin-4 has direct effects on peripheral nerves that are independent of its antihyperglycemic and hemodynamic effects.

Several antibodies against the GLP-1R are commercially available. GLP-1R antibodies, LS-A1205 and LS-A1206, produced by MBL International, have recently been used in some studies (26–28). To confirm the reliability of these antibodies, we stained islet cells in which the presence of the GLP-1R has repeatedly been demonstrated (29,30). LS-A1205 and LS-A1206 distinctively reacted with β-cells that also were clearly stained with anti-insulin antibody, but these antisera also reacted with β-cells or perhaps α-cells in Glp1r$^{-/-}$ mice. We then tested another antibody for GLP-1R, sc-66911 (Santa Cruz). This antiserum detected β-cells

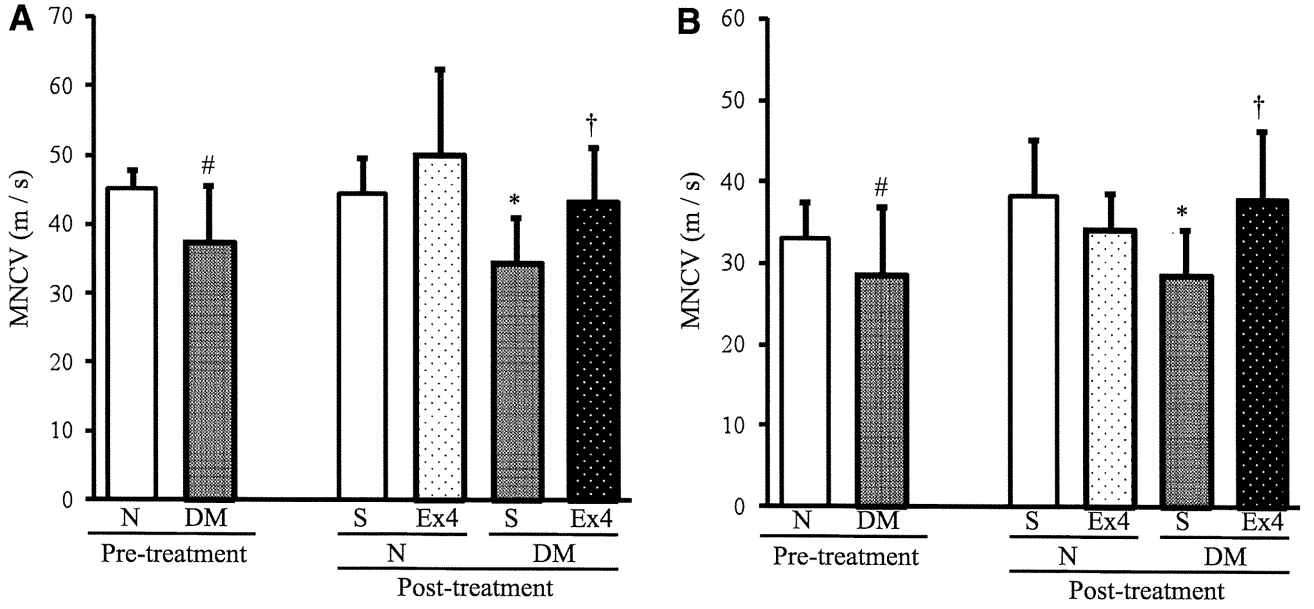

FIG. 5. NCVs. MNCV (*A*) and SNCV (*B*) were measured before and after the treatment with exendin-4 (Ex4). DM, diabetic mice; N, normal mice; S, saline. Before the treatment: MNCV for normal mice 45.2 ± 2.7 m/s and diabetic mice 37.5 ± 8.2, $P = 0.0341$; SNCV for normal mice 33.0 ± 4.6 and diabetic mice 28.6 ± 7.2, $P = 0.0489$. After the treatment: MNCV for saline-treated diabetic mice 34.5 ± 8.1 and exendin-4–treated diabetic mice 43.3 ± 7.9, $P = 0.0289$; SNCV for saline-treated diabetic mice 28.6 ± 5.6 and exendin-4–treated diabetic mice 38.0 ± 8.5, $P = 0.0201$. Results are means ± SD. #$P < 0.05$ vs. pretreatment normal mice. *$P < 0.05$ vs. saline-treated normal mice. †$P < 0.05$ vs. saline-treated diabetic mice. Saline-treated normal mice, $n = 7$; exendin-4–treated normal mice, $n = 8$; saline-treated diabetic mice, $n = 8$; exendin-4–treated diabetic mice, $n = 8$.

of wild-type mice but did not react with those of *glp1r*$^{-/-}$ mice (Supplementary Fig. 1). Furthermore, the antiserum detected GLP-1R proteins in the pancreata of wild-type mice but not in that of *glp1r*$^{-/-}$ mice, using immunoblotting assay. We confirmed the expression of GLP-1R in DRG neurons and glia cells with a GLP-1R antibody, sc-66911.

GLP-1 and exendin-4 previously have been shown to promote neurite outgrowth of rat pheochromocytoma cells (19,31) and to protect rat primary hippocampal neurons from cell death (14). It has been reported that exogenous GLP-1R activation significantly reduces glucose-dependent reactive oxygen species generation in hypothalamus (32). These antioxidative effects of GLP-1R agonists might yield benefits to central and peripheral nervous systems.

The dipeptidyl peptidase (DPP)-IV inhibitor (vildagliptin) recently has been shown to prevent peripheral nerve degeneration in STZ-induced diabetic mice (33). Although GLP-1 is one of the substrates of DPP-IV, several bioactive peptides, such as neuropeptide Y, substance P, glucagon-like peptide-2, and stromal cell–derived factor-1α also have been reported as substrates of DPP-IV (34,35). Among these peptides, neuropeptide Y and substance P are known as neurotransmitters or modulators of peripheral nervous systems (36,37), and it also has been demonstrated that stromal cell–derived factor-1α released from DRG glia regulates leukocyte chemotaxis and modulates neuropathic pain behavior (38). Therefore, the preventive effects of the DPP-IV inhibitor on DPN may be attributed to its protective effects on these neurotrophic peptides and mediated through increased levels of GLP-1.

Although we cannot infer the precise site(s) of action of exendin-4 in our diabetic mice that ameliorated DPN in vivo, our data using cellular models of DPN in vitro implicate a direct role for GLP-1 and the GLP-1R agonist exendin-4. We previously reported that conditioned media obtained from Schwann cell cultures under high-glucose conditions impaired neurite outgrowth of DRG neurons, likely mediated through a decrease in nerve growth factor production (21). In our current study, the impaired neurite outgrowth induced by hyperglycemia-conditioned IMS media was improved by exendin-4. In contrast, under the normal glucose–conditioned IMS media, which mimicked the nondiabetic normal state, exendin-4 did not exert any changes in neurite outgrowth because of basal enhancement of neurite outgrowth by various growth factors, such as nerve growth factor secreted from Schwann cells (21). These results indicate that GLP-1R agonists exert regenerative effects on peripheral sensory neurons under experimental conditions, mimicking diabetes in vitro. Additional studies on the effect on the role of downstream neurotrophic factors, such as nerve growth factor, will be required to evaluate the mechanism of action of GLP-1R agonists.

We also demonstrated the effects of exendin-4 on DPN in STZ-induced diabetic mice. We evaluated sensory nerve functions using a CPT/laboratory neurometer. The neurometer is now widely and clinically used to evaluate the effects of analgesic drugs and peripheral nerve functions in various painful neuropathies, including DPN (39–42). In this study, after 12 weeks of diabetes, hypoalgesia at 2,000, 250, and 5 Hz was observed in the diabetic mice, and injection of exendin-4 improved these abnormalities. In addition, exendin-4 ameliorated the decreased IENFDs in diabetic mice. The restoration of sensory functions by exendin-4 was confirmed by the improvement of IENFDs.

In addition, we measured MNCVs and SNCVs that represent relatively large axonal functions. Both the delayed MNCVs and SNCVs in diabetic mice were improved by exendin-4, indicating that exendin-4 had therapeutic effects on impaired motor and sensory nerve functions. These data also are consistent with previous reports (14,16,18,19) that revealed the plausible effects of GLP-1 or GLP-1R agonists on central and peripheral nerve disorders.

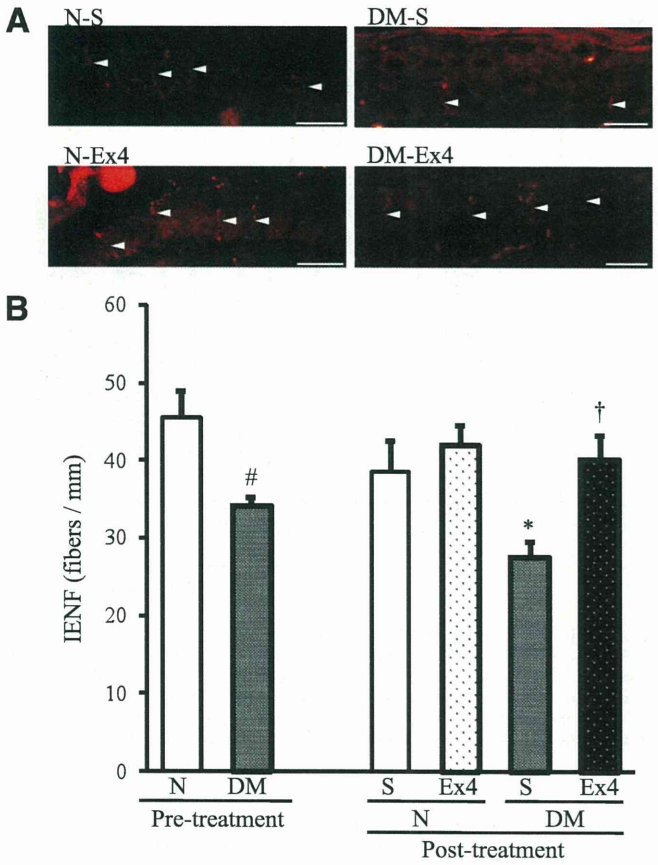

FIG. 6. IENFDs after the treatment with exendin-4 (Ex4). *A*: IENFs indicated by white arrowheads were detected by immunofluorescence assay with anti–PGP 9.5 antibody (red). *B*: Quantification of the density revealed a significant decrement in untreated diabetic mice and the significant amelioration by exendin-4 treatment. DM, diabetic mice; N, normal mice; S, saline. Bar: 20 μm. Saline-treated normal mice 38.5 ± 3.9, saline-treated diabetic mice 27.7 ± 1.9, exendin-4–treated normal mice 42.1 ± 2.4, and exendin-4–treated diabetic mice 40.2 ± 3.1 fibers per mm. Results are means ± SD. #$P < 0.05$ vs. pretreatment normal mice. *$P < 0.05$ vs. saline-treated normal mice. †$P < 0.05$ vs. saline-treated diabetic mice. Saline-treated normal mice, $n = 4$; exendin-4–treated normal mice, $n = 3$; saline-treated diabetic mice, $n = 4$; exendin-4–treated diabetic mice, $n = 3$. (A high-quality digital representation of this figure is available in the online issue.)

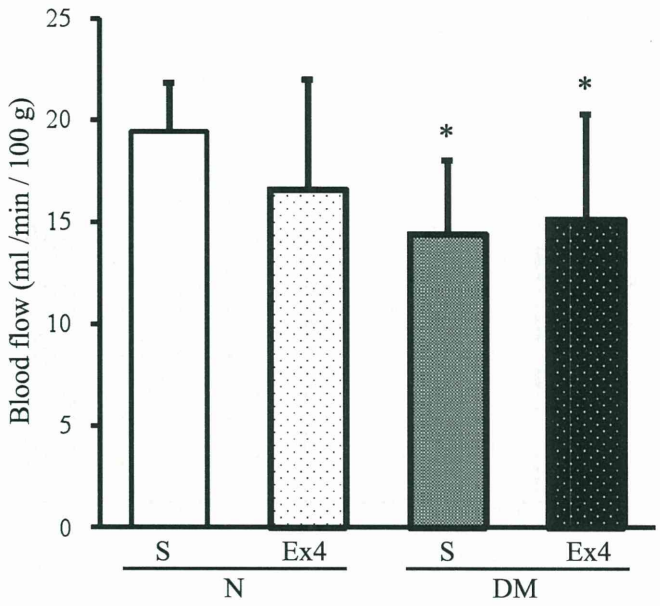

FIG. 7. SNBF treated with or without exendin-4 (Ex4) in normal (N) or diabetic (DM) mice. S, saline. Saline-treated normal mice 19.4 ± 2.4, saline-treated diabetic mice 14.4 ± 3.6, and exendin-4–treated diabetic mice 15.2 ± 5.2 mL/min/100 g. Results are means ± SD. *$P < 0.05$ vs. saline-treated normal mice. Saline-treated normal mice, $n = 9$; exendin-4–treated normal mice, $n = 8$; saline-treated diabetic mice, $n = 8$; exendin-4–treated diabetic mice, $n = 9$.

Decreased nerve blood flow has been recognized as one of the most important mechanisms in the development of DPN. Recently, GLP-1R has been detected in blood vessels, and the beneficial effects of GLP-1 or GLP-1R agonists on vascular functions have been reported (28,43,44). In our experimental study, however, exendin-4 did not alter normal nerve blood flow in normal mice nor did it improve the reduced nerve blood flow in diabetic mice. One of the reasons for this discrepancy is that the vasodilatory actions of GLP-1 agonists are likely mediated mainly through a GLP-1R–independent pathway, which depends on a GLP-1 metabolite, GLP-1 (9–36) (28). In our present study, therefore, exendin-4 could not exert vasoregulatory effects. Another reason is that the central-peripheral sympathetic nervous system function would likely be impaired in the diabetic state. It has been reported that GLP-1 in the central nervous system regulates sympathetic outflow, resulting in increases in blood pressure and heart rate independent of the peripheral actions of GLP-1 on glucoregulation (43,44). As mice with a long duration of diabetes in the current study might have developed sympathetic nerve dysfunction, exendin-4 may have been unable to modulate nerve blood flow after prolonged experimental diabetes. Although the precise mechanisms remain unclear, the effects of exendin-4 on DPN may be attributed to its direct actions on DRG neurons and their axons.

Because GLP-1R agonists possess glucose-lowering effects, we used a dosing regimen that did not produce sustained reductions in blood glucose or body weight. Although trends toward reduced levels of HbA_{1c} and glucagon were observed in exendin-4–treated diabetic mice (Table 1 and Supplementary Fig. 4), there were no significant differences in the glucose levels, insulin concentrations, or IPGTTs between exendin-4–treated and untreated mice. In previous studies (45,46), exendin-4 was administrated at the same time as or before STZ injection. On the other hand, we started exendin-4 injections 12 weeks after the onset of diabetes. Because HbA_{1c} in diabetic mice treated with exendin-4 tended to decrease (Table 1), longer treatment or larger doses of exendin-4 might have significantly improved hyperglycemia, indirectly contributing to the amelioration of DPN. In the current study, however, it is conceivable that the effectiveness of exendin-4 on DPN may be independent of the glucose-lowering effects.

Miki et al. (47) previously reported that glucose-responsive neurons in the hypothalamus regulate the secretion of glucagon and govern the glucose homeostasis. In addition, it was shown in a recent study that GLP-1R agonists had a glucagon-lowering effect (48), which is consistent with the present observation that glucagon concentrations tended to be decreased by the administration of exendin-4 in diabetic mice. It remains to be evaluated whether the glucagon levels influence the pathophysiology of DPN through mechanisms independent of hyperglycemia.

In conclusion, we demonstrated the beneficial effects of GLP-1R agonist on DPN. GLP-1 analogs and GLP-1R

agonists have been broadly used as antihyperglycemic agents in type 2 diabetic patients. In addition to the established use of these agents to control blood glucose, there currently is little data demonstrating an effect of GLP-1R agonists on peripheral nerve functions. Our data demonstrating the improvement of experimental DPN after administration of GLP-1 and exendin-4 suggest that additional clinical investigation with attention to whether therapy with GLP-1R agonists produce changes in DPN may be warranted.

ACKNOWLEDGMENTS

This research was supported in part by a grant-in-aid for scientific research (21592506) from the Ministry of Education, Culture, Sports, Science, and Technology (MEXT) and in part by the "Strategic Research AGU-Platform Formation (2008–2012)" Project for Private Universities: matching fund subsidy from MEXT of Japan.

No potential conflicts of interest relevant to this article were reported.

T.H. researched data. H.K. designed the animal and cell culture studies and contributed to the writing and editing of the manuscript. K.N. contributed to discussion. N.H. was responsible for the maintenance of the animals. N.O. and Yus.S. contributed to discussion. T.S. and M.K. reviewed the manuscript. J.K., T.O., and A.F. researched data. Y.H. contributed to discussion. N.I. was responsible for the maintenance of the animals. Yut.S. and D.J.D. wrote, reviewed, and edited the manuscript. Y.O. contributed to discussion. J.N. wrote, reviewed, and edited the manuscript.

The authors thank Michiko Yamada, Keiko Shimamoto, Naoko Furukawa, Chikako Nagase, and Mayumi Katagiri, from the Department of Endocrinology and Diabetes, Nagoya University Graduate School of Medicine, for technical assistance.

REFERENCES

1. Toth C, Brussee V, Cheng C, Zochodne DW. Diabetes mellitus and the sensory neuron. J Neuropathol Exp Neurol 2004;63:561–573
2. Zochodne DW. Diabetes mellitus and the peripheral nervous system: manifestations and mechanisms. Muscle Nerve 2007;36:144–166
3. Kles KA, Vinik AI. Pathophysiology and treatment of diabetic peripheral neuropathy: the case for diabetic neurovascular function as an essential component. Curr Diabetes Rev 2006;2:131–145
4. Genuth S. Insights from the diabetes control and complications trial/epidemiology of diabetes interventions and complications study on the use of intensive glycemic treatment to reduce the risk of complications of type 1 diabetes. Endocr Pract 2006;12(Suppl. 1):34–41
5. Nakae M, Kamiya H, Naruse K, et al. Effects of basic fibroblast growth factor on experimental diabetic neuropathy in rats. Diabetes 2006;55:1470–1477
6. Naruse K, Hamada Y, Nakashima E, et al. Therapeutic neovascularization using cord blood-derived endothelial progenitor cells for diabetic neuropathy. Diabetes 2005;54:1823–1828
7. Shibata T, Naruse K, Kamiya H, et al. Transplantation of bone marrow-derived mesenchymal stem cells improves diabetic polyneuropathy in rats. Diabetes 2008;57:3099–3107
8. Drucker DJ, Nauck MA. The incretin system: glucagon-like peptide-1 receptor agonists and dipeptidyl peptidase-4 inhibitors in type 2 diabetes. Lancet 2006;368:1696–1705
9. Lovshin JA, Drucker DJ. Incretin-based therapies for type 2 diabetes mellitus. Nat Rev Endocrinol 2009;5:262–269
10. Gutniak M, Orskov C, Holst JJ, Ahrén B, Efendic S. Antidiabetogenic effect of glucagon-like peptide-1 (7-36)amide in normal subjects and patients with diabetes mellitus. N Engl J Med 1992;326:1316–1322
11. Dupre J, Behme MT, Hramiak IM, et al. Glucagon-like peptide I reduces postprandial glycemic excursions in IDDM. Diabetes 1995;44:626–630
12. Turton MD, O'Shea D, Gunn I, et al. A role for glucagon-like peptide-1 in the central regulation of feeding. Nature 1996;379:69–72
13. Hansotia T, Maida A, Flock G, et al. Extrapancreatic incretin receptors modulate glucose homeostasis, body weight, and energy expenditure. J Clin Invest 2007;117:143–152
14. Perry T, Lahiri DK, Sambamurti K, et al. Glucagon-like peptide-1 decreases endogenous amyloid-beta peptide (Abeta) levels and protects hippocampal neurons from death induced by Abeta and iron. J Neurosci Res 2003;72:603–612
15. During MJ, Cao L, Zuzga DS, et al. Glucagon-like peptide-1 receptor is involved in learning and neuroprotection. Nat Med 2003;9:1173–1179
16. Bertilsson G, Patrone C, Zachrisson O, et al. Peptide hormone exendin-4 stimulates subventricular zone neurogenesis in the adult rodent brain and induces recovery in an animal model of Parkinson's disease. J Neurosci Res 2008;86:326–338
17. Belsham DD, Fick LJ, Dalvi PS, et al. Ciliary neurotrophic factor recruitment of glucagon-like peptide-1 mediates neurogenesis, allowing immortalization of adult murine hypothalamic neurons. FASEB J 2009;23:4256–4265
18. Li Y, Perry T, Kindy MS, et al. GLP-1 receptor stimulation preserves primary cortical and dopaminergic neurons in cellular and rodent models of stroke and Parkinsonism. Proc Natl Acad Sci USA 2009;106:1285–1290
19. Perry T, Lahiri DK, Chen D, et al. A novel neurotrophic property of glucagon-like peptide 1: a promoter of nerve growth factor-mediated differentiation in PC12 cells. J Pharmacol Exp Ther 2002;300:958–966
20. Perry T, Holloway HW, Weerasuriya A, et al. Evidence of GLP-1-mediated neuroprotection in an animal model of pyridoxine-induced peripheral sensory neuropathy. Exp Neurol 2007;203:293–301
21. Watabe K, Fukuda T, Tanaka J, Honda H, Toyohara K, Sakai O. Spontaneously immortalized adult mouse Schwann cells secrete autocrine and paracrine growth-promoting activities. J Neurosci Res 1995;41:279–290
22. Tosaki T, Kamiya H, Yasuda Y, et al. Reduced NGF secretion by Schwann cells under the high glucose condition decreases neurite outgrowth of DRG neurons. Exp Neurol 2008;213:381–387
23. Nakamura J, Kato K, Hamada Y, et al. A protein kinase C-β–selective inhibitor ameliorates neural dysfunction in streptozotocin-induced diabetic rats. Diabetes 1999;48:2090–2095
24. Livak KJ, Schmittgen TD. Analysis of relative gene expression data using real-time quantitative PCR and the 2(-Delta Delta C(T)) Method. Methods 2001;25:402–408
25. Beiswenger KK, Calcutt NA, Mizisin AP. Epidermal nerve fiber quantification in the assessment of diabetic neuropathy. Acta Histochem 2008;110:351–362
26. Arakawa M, Mita T, Azuma K, et al. Inhibition of monocyte adhesion to endothelial cells and attenuation of atherosclerotic lesion by a glucagon-like peptide-1 receptor agonist, exendin-4. Diabetes 2010;59:1030–1037
27. Tornehave D, Kristensen P, Rømer J, Knudsen LB, Heller RS. Expression of the GLP-1 receptor in mouse, rat, and human pancreas. J Histochem Cytochem 2008;56:841–851
28. Ban K, Noyan-Ashraf MH, Hoefer J, Bolz SS, Drucker DJ, Husain M. Cardioprotective and vasodilatory actions of glucagon-like peptide 1 receptor are mediated through both glucagon-like peptide 1 receptor-dependent and -independent pathways. Circulation 2008;117:2340–2350
29. Thorens B. Expression cloning of the pancreatic beta cell receptor for the gluco-incretin hormone glucagon-like peptide 1. Proc Natl Acad Sci USA 1992;89:8641–8645
30. Montrose-Rafizadeh C, Avdonin P, Garant MJ, et al. Pancreatic glucagon-like peptide-1 receptor couples to multiple G proteins and activates mitogen-activated protein kinase pathways in Chinese hamster ovary cells. Endocrinology 1999;140:1132–1140
31. Kimura R, Okouchi M, Fujioka H, et al. Glucagon-like peptide-1 (GLP-1) protects against methylglyoxal-induced PC12 cell apoptosis through the PI3K/Akt/mTOR/GCLc/redox signaling pathway. Neuroscience 2009;162:1212–1219
32. Cabou C, Campistron G, Marsollier N, et al. Brain glucagon-like peptide-1 regulates arterial blood flow, heart rate, and insulin sensitivity. Diabetes 2008;57:2577–2587
33. Jin HY, Liu WJ, Park JH, Baek HS, Park TS. Effect of dipeptidyl peptidase-IV (DPP-IV) inhibitor (Vildagliptin) on peripheral nerves in streptozotocin-induced diabetic rats. Arch Med Res 2009;40:536–544
34. Mentlein R. Dipeptidyl-peptidase IV (CD26): role in the inactivation of regulatory peptides. Regul Pept 1999;85:9–24
35. De Meester I, Durinx C, Bal G, et al. Natural substrates of dipeptidyl peptidase IV. Adv Exp Med Biol 2000;477:67–87
36. Allen BJ, Rogers SD, Ghilardi JR, et al. Noxious cutaneous thermal stimuli induce a graded release of endogenous substance P in the spinal cord: imaging peptide action in vivo. J Neurosci 1997;17:5921–5927
37. Ji RR, Zhang X, Wiesenfeld-Hallin Z, Hökfelt T. Expression of neuropeptide Y and neuropeptide Y (Y1) receptor mRNA in rat spinal cord and dorsal root ganglia following peripheral tissue inflammation. J Neurosci 1994;14:6423–6434
38. White FA, Jung H, Miller RJ. Chemokines and the pathophysiology of neuropathic pain. Proc Natl Acad Sci USA 2007;104:20151–20158

39. Katims JJ, Naviasky EH, Ng LK, Rendell M, Bleecker ML. New screening device for assessment of peripheral neuropathy. J Occup Med 1986;28: 1219–1221
40. Masson EA, Veves A, Fernando D, Boulton AJ. Current perception thresholds: a new, quick, and reproducible method for the assessment of peripheral neuropathy in diabetes mellitus. Diabetologia 1989;32:724–728
41. Veves A, Young MJ, Manes C, Boulton AJ. Differences in peripheral and autonomic nerve function measurements in painful and painless neuropathy: a clinical study. Diabetes Care 1994;17:1200–1202
42. Matsutomo R, Takebayashi K, Aso Y. Assessment of peripheral neuropathy using measurement of the current perception threshold with the neurometer in patients with type 2 diabetes mellitus. J Int Med Res 2005;33:442–453
43. Yamamoto H, Lee CE, Marcus JN, et al. Glucagon-like peptide-1 receptor stimulation increases blood pressure and heart rate and activates autonomic regulatory neurons. J Clin Invest 2002;110:43–52
44. Barragán JM, Eng J, Rodríguez R, Blázquez E. Neural contribution to the effect of glucagon-like peptide-1-(7-36) amide on arterial blood pressure in rats. Am J Physiol 1999;277:E784–E791
45. Li Y, Hansotia T, Yusta B, Ris F, Halban PA, Drucker DJ. Glucagon-like peptide-1 receptor signaling modulates beta cell apoptosis. J Biol Chem 2003;278:471–478
46. Maida A, Hansotia T, Longuet C, Seino Y, Drucker DJ. Differential importance of glucose-dependent insulinotropic polypeptide vs glucagon-like peptide 1 receptor signaling for beta cell survival in mice. Gastroenterology 2009;137:2146–2157
47. Miki T, Liss B, Minami K, et al. ATP-sensitive K+ channels in the hypothalamus are essential for the maintenance of glucose homeostasis. Nat Neurosci 2001;4:507–512
48. Burcelin R, Knauf C, Cani PD. Pancreatic alpha-cell dysfunction in diabetes. Diabetes Metab 2008;34(Suppl. 2):S49–S55

Ionic mechanisms and Ca^{2+} dynamics underlying the glucose response of pancreatic β cells: a simulation study

Chae Young Cha,[1] Yasuhiko Nakamura,[2] Yukiko Himeno,[2] JianWu Wang,[3] Shinpei Fujimoto,[2] Nobuya Inagaki,[2] Yung E Earm,[4] and Akinori Noma[1]

[1]Biosimulation Project, Faculty of Bioinformatics, Ritsumeikan University, Kusatsu, Shiga 525-8577, Japan
[2]Department of Diabetes and Clinical Nutrition, Graduate School of Medicine, Kyoto University, Kyoto 606-8501, Japan
[3]School of Public Health, Central South University, Changsha 410078, China
[4]Department of Physiology, Seoul National University, Seoul 110-749, Korea

To clarify the mechanisms underlying the pancreatic β-cell response to varying glucose concentrations ([G]), electrophysiological findings were integrated into a mathematical cell model. The Ca^{2+} dynamics of the endoplasmic reticulum (ER) were also improved. The model was validated by demonstrating quiescent potential, burst–interburst electrical events accompanied by Ca^{2+} transients, and continuous firing of action potentials over [G] ranges of 0–6, 7–18, and >19 mM, respectively. These responses to glucose were completely reversible. The action potential, input impedance, and Ca^{2+} transients were in good agreement with experimental measurements. The ionic mechanisms underlying the burst–interburst rhythm were investigated by lead potential analysis, which quantified the contributions of individual current components. This analysis demonstrated that slow potential changes during the interburst period were attributable to modifications of ion channels or transporters by intracellular ions and/or metabolites to different degrees depending on [G]. The predominant role of adenosine triphosphate–sensitive K^+ current in switching on and off the repetitive firing of action potentials at 8 mM [G] was taken over at a higher [G] by Ca^{2+}- or Na^+-dependent currents, which were generated by the plasma membrane Ca^{2+} pump, Na^+/K^+ pump, Na^+/Ca^{2+} exchanger, and TRPM channel. Accumulation and release of Ca^{2+} by the ER also had a strong influence on the slow electrical rhythm. We conclude that the present mathematical model is useful for quantifying the role of individual functional components in the whole cell responses based on experimental findings.

INTRODUCTION

The pancreatic β cell has a unique function of converting variations in the extracellular glucose concentration ([G]) to electrical activity, thereby controlling the level of insulin secretion. This signal transduction is dependent on the interaction between energy metabolism and membrane excitation. Several mechanisms have been suggested underlying this bilateral coupling in pancreatic β cells. The gating of ATP-sensitive K^+ channels is regulated by fluctuations in the intracellular concentration of ATP or MgADP ([ATP] or [MgADP]), resulting in a prolongation of the duration of the burst of action potentials with increasing [G]. The activation of L-type Ca^{2+} channels by an increase of [ATP] (Smith et al., 1989), or the depression of Na^+/K^+ pump (NaK) activity up to 50% by increasing [G] (Owada et al., 1999), may also favor burst prolongation. In addition, variations in intracellular ion concentrations may have varying influences on individual channels or transporters depending on [G]. For example, it has been recently suggested that a K^+ current activated by intracellular Ca^{2+} (I_{Kslow}) may affect bursting activity (Göpel et al., 1999a; Goforth et al., 2002). Finally, the electrical activity induces a significant increase in ion fluxes across the surface membrane, which alters energy consumption via active ion transport or Ca^{2+}-mediated processes, including insulin secretion. These pathways are all linked in a complex system, and one approach to aid the quantification of the contribution to bursting activity of individual pathways is the development of a mathematical β-cell model.

Such models have been used for nearly 30 years to elucidate the principle mechanisms underlying the bursting activity in β cells. Early stage models used a formulation consisting of a minimum number of components: two or three K^+ currents, a Ca^{2+} current, and/or a leak current (Chay and Keizer, 1983; Sherman et al., 1988, 1990; Keizer and Magnus, 1989; Smolen and Keizer, 1992; Bertram et al., 1995b). These model simulations suggested consistently the critical role of a slowly changing variable in generating the burst–interburst

C.Y. Cha and Y. Nakamura contributed equally to this paper.
Correspondence to Akinori Noma: noma@sk.ritsumei.ac.jp

Abbreviations used in this paper: BK, large-conductance Ca^{2+}-activated K^+; NaK, Na^+/K^+ pump; NCX, Na^+/Ca^{2+} exchange; PMCA, plasma membrane Ca^{2+} pump; SERCA, ER Ca^{2+} ATPase; SK, small-conductance K_{Ca}; TCA, tricarboxylic acid.

The Rockefeller University Press $30.00
J. Gen. Physiol. Vol. 138 No. 1 21–37
www.jgp.org/cgi/doi/10.1085/jgp.201110611

rhythm. Subsequent models elaborated metabolic components by including details of glycolysis, tricarboxylic acid (TCA) cycle, and oxidative phosphorylation (Magnus and Keizer, 1998; Bertram et al., 2004; Diederichs, 2006) to examine the gating of I_{KATP} by time-dependent changes in [ADP] or glycolytic oscillation. Several models with detailed descriptions of many more membrane currents and associated changes in intracellular ion concentrations have also been published (Miwa and Imai, 1999; Fridlyand et al., 2003; Meyer-Hermann, 2007).

The object of this study is to clarify quantitatively the detailed ionic mechanisms underlying glucose-induced electrical bursting activity observed in isolated β cells. To achieve this aim, we have developed a comprehensive model based on recent extensive experimental findings on ion channels, transporters, and intracellular Ca^{2+} dynamics in β cells. If adequate mathematical analyses are successfully applied to this detailed model, the role of individual ion channels will be clarified in quantitative terms, in relation to the principle mechanisms deduced from the theoretical studies using simplified models, and also in relation to the detailed experimental studies on the role of individual functional molecules in real cells.

MATERIALS AND METHODS

The present model of a single β cell was constructed on the framework developed by Fridlyand, Philipson, and their colleagues, the FP model (Fridlyand et al., 2003, 2005), which was designed to examine interactions among glucose metabolism, Ca^{2+} dynamics including ER, and membrane excitation. The metabolic elements of the model were adopted after minor modifications, whereas the formulations of individual ion channels and transporters were largely revised to reproduce the detailed characteristics of electrical activities reported in the literature. The structure of the model is illustrated in Fig. 1. Because electrical activities or glucose sensitivities vary diversely among different studies or species, we have concentrated on data obtained from dissociated mouse β cells at physiological temperature (33–37°C). Experimental results from other species, including rat and human, or obtained at room temperature were also referred in the absence of relevant mouse data. All equations and parameters are presented in the supplemental material.

Cell dimensions and Ca^{2+} buffer

Cytosolic (764 fl) and ER (280 fl) volumes and membrane capacitance (6.158 pF) were defined as in the FP model (Fridlyand et al., 2003). This capacitance is within the experimental range measured in isolated β cells in mouse (5.4 ± 0.9 pF) (Rorsman and Trube, 1986) and similar to that found in humans (6.2 ± 0.8 or 7.3 ± 0.4 pF) (Kelly et al., 1991). The concentrations of free Ca^{2+} in the cytosol ($[Ca^{2+}]_i$) and ER ($[Ca^{2+}]_{ER}$) were calculated using the buffering power coefficients f_i and f_{ER}, respectively (see Eqs. S5 and S6 in the supplemental material). The value of f_{ER} was determined using the decay time course of the Ca^{2+} transient evoked by a 45-mM K^+ pulse (Gilon et al., 1999), assuming an ER Ca^{2+}-binding capacity of 98–99% as found in gonadotropes (Tse et al., 1994).

Modeling ion channels and transporters

Plasma membrane ion transport comprised eight ion channels and three ion transporters as indicated in Fig. 1. Modeling parameters were based on voltage-clamp data obtained mainly in dissociated β cells, as indicated.

Voltage-dependent Ca^{2+} current (I_{CaV}). It is well established that the maximum rate of rise of action potential is determined by the activation of voltage (V)-dependent Ca^{2+} currents in pancreatic β cells (Ribalet and Beigelman, 1980; Rorsman and Trube, 1986; Ashcroft and Rorsman, 1989). Several types of voltage-gated Ca^{2+} channels (L, R, and possibly P/Q type) have been reported in mouse β cells (Schulla et al., 2003). Braun et al. (2008) also demonstrated that human β cells express L, T, and P/Q types, but not R-type Ca^{2+} channels. At present, it is not possible to describe quantitatively each component because of the lack of detailed voltage-clamp data from isolated cells. However, the whole cell Ca^{2+} currents so far reported show common characteristics for L-type Ca^{2+} current established in other cell types. These include Ca^{2+}-mediated inactivation (Plant, 1988; Satin and Cook, 1989; Kelly et al., 1991), ultraslow V-dependent inactivation (Satin and Cook, 1989; Kelly et al., 1991), and activation by intracellular ATP (Smith et al., 1989) or "washout" with an ATP-free pipette solution (Hiriart and Matteson, 1988). All of these properties might be heavily involved in modulation of membrane excitability. For example, Henquin and Meissner (1984a) ascribed a gradual decrease in the amplitude and frequency of Ca^{2+} spikes to Ca^{2+}- and ultraslow V-dependent inactivation of I_{CaV} during the burst. As an initial approximation, we have used a lumped Ca^{2+} current with characteristics similar to those of L-type Ca^{2+} current described by a formulation of I_{CaL} developed in cardiac myocytes (Takeuchi et al., 2006). The parameters were adjusted according to voltage-clamp experiments in an insulin-secreting cell line (Satin and Cook, 1989; see Fig. S1) and in isolated mouse β cells (Houamed et al., 2010). Because the kinetics of Ca^{2+} current of human β cells are

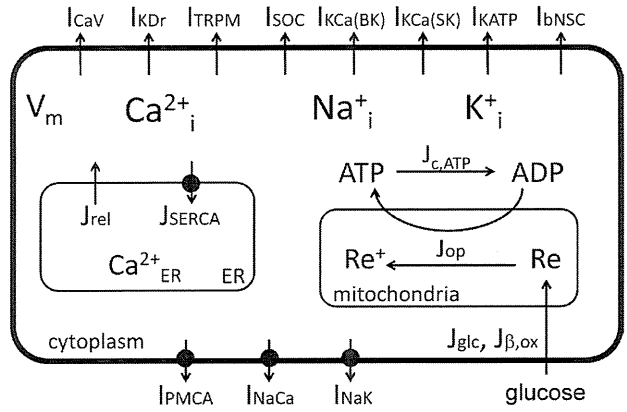

Figure 1. Schematic diagram of the new β-cell model. The model includes ion fluxes through the plasma membrane, Ca^{2+} dynamics including the ER, and [G]-dependent ATP synthesis in mitochondria. The ion fluxes include voltage-dependent Ca^{2+} current (I_{CaV}), delayed rectifier K^+ current (I_{KDr}), Ca^{2+}-activated nonselective cation current (I_{TRPM}), store-operated current (I_{SOC}), V- and $[Ca^{2+}]_i$-dependent transient outward K^+ current ($I_{KCa(BK)}$), ATP-sensitive K^+ current (I_{KATP}), Ca^{2+}-activated K^+ current ($I_{KCa(SK)}$), background nonselective cation current (I_{bNSC}), PMCA current (I_{PMCA}), NCX current (I_{NaCa}), and NaK current (I_{NaK}). ER Ca^{2+} dynamics consist of Ca^{2+} uptake by SERCA (J_{SERCA}) and Ca^{2+} release (J_{rel}). In the ATP synthesis pathway, Re represents the reduced form of pyridine nucleotide (NADH), and J_{glc} and $J_{\beta,ox}$ represent the glycolysis- and β oxidation–dependent Re production rates, respectively. ATP is synthesized at the expense of Re through oxidative phosphorylation (J_{op}) and is consumed via Ca^{2+}-dependent/-independent pathways ($J_{c,ATP}$). The direction of arrows indicates the positive sign of the values calculated by the corresponding equations in the supplemental material.

similar to those in rodent (Kelly et al., 1991), human data were also used for determining the voltage-dependent activation curve and the time course of ultraslow inactivation. Ca^{2+}-dependent inactivation was described as a function of the single-channel current (Eqs. S18 and S19). For ultraslow inactivation, a noninactivating fraction of 0.4 (Eq. S13) was assumed to reproduce the inactivation curve obtained with a 10-s conditioning pulse (Fig. S1 F). Ideally, all of these properties might better be systematically analyzed in a single study at the physiological temperature. Such a study is awaited.

Delayed rectifier K^+ current (I_{KDr}). Pancreatic β cells show a marked delayed outward K^+ current on depolarization (Cook and Hales, 1984; Rorsman and Trube, 1986; Smith et al., 1990b). The voltage-clamp record of I_{KDr} in dissociated β cells of mouse (Houamed et al., 2010) was reproduced (Fig. S2, A and B). For a more precise description of the activation gate (Eqs. S26 and S27), the I-V relationship and activation curve obtained from human (Kelly et al., 1991) and mouse β cells (Rorsman and Trube, 1986) were also considered (Fig. S2 C). In addition, a slow inactivation of I_{KDr} has been observed in various studies (Rorsman and Trube, 1986; Kelly et al., 1991; Houamed et al., 2010). Because the inactivation kinetics were highly dependent on temperature (MacDonald et al., 2003), a time constant of ~0.3 s at +10 mV at 32–35°C (Houamed et al., 2010) was used for model adjustment (Eqs. S29 and S30).

Ca^{2+}-activated nonselective cation current (I_{TRPM}). Sturgess et al. (1987) recorded single-channel currents of a Ca^{2+}-activated nonselective cation channel in the INS-1 cell line. Recently, an analogous but more specific current has been described as a TRPM4 channel current, which might be involved in insulin secretion (Cheng et al., 2007; Marigo et al., 2009). In spite of the recent findings, this channel has not been implemented in previous β-cell models. We described the activation by Ca^{2+} (Eq. S48) with a half-saturation concentration (0.76 μM) and a Hill coefficient (1.7), consistent with experimental recordings (Marigo et al., 2009). The relative permeabilities of Na^+ and K^+ (Eqs. S50 and S51) were adjusted to give a reversal potential of ~0 mV (Colsoul et al., 2010). The whole cell conductance of I_{TRPM} was adjusted to reconstruct the plateau potential of approximately −50 mV during the burst.

Store-operated current (I_{SOC}). Worley et al. (1994a,b) showed that depletion of ER Ca^{2+} store by zero Ca^{2+} bath solution with EGTA depolarized the membrane in freshly isolated mouse β cells. They also demonstrated that a nonselective cation current was activated by maitotoxin. Leech and Habener (1998) also recorded a similar maitotoxin-sensitive current that showed a reversal potential of −1.7 mV in insulinoma cell lines. The authors suggested that this current might play a critical role in setting the membrane potential (V_m) to be less negative than the K^+ equilibrium potential. Unfortunately, it is still unknown if the store-operated cation currents are attributable to a single class of ion channels at the molecular level. Moreover, the critical level of ER Ca^{2+} depletion for the half-activation of the store-operated currents ($K_{0.5,ER}$) remains unclear in β cells. Although a Ca^{2+} release–activated nonselective cation (CRAN) current has been implemented in previous β-cell models (Bertram et al., 1995a; Chay, 1996, 1997; Mears et al., 1997; Fridlyand et al., 2003), different values of $K_{0.5,ER}$ ranging from 3 to 200 μM were used. In our model, the minimum level of 3 μM $[Ca^{2+}]_{ER}$ is tentatively assumed for the half-activation (Eq. S44). With this assumption, the amplitude of I_{SOC} is minimum under the physiological conditions, but it is activated when the ER is almost completely depleted, for example, by applying thapsigargin.

Miura et al. (1997) demonstrated that depletion of Ca^{2+} store by thapsigargin triggered Ca^{2+} influx independent of I_{CaV}, which might be attributed to a different type of current from I_{CRAN}. Based on their finding, I_{SOC} in our model is partly carried by Ca^{2+}, and the size of the current was determined by the steady-state level of $[Ca^{2+}]_i$ under thapsigargin and D_{600}, a blocker of I_{CaV} (Eq. S47). It is consistent with the fact that ubiquitous Ca^{2+} release–activated Ca^{2+} (CRAC) channels are selective to Ca^{2+} under physiological ionic conditions (Hoth and Penner, 1993; Prakriya and Lewis, 2002). This Ca^{2+} entry prevents ER from a serious depletion at 0 mM [G] in our model, and the Na^+ and K^+ conductance of I_{SOC} sets the resting membrane potential at approximately −70 mV in competition with the background of I_{KATP} (Eqs. S45 and S46).

V- and $[Ca^{2+}]_i$-dependent transient outward K^+ current ($I_{KCa(BK)}$). A large-conductance Ca^{2+}-activated K^+ (BK) current has been recorded in single-channel recordings in insulin-secreting cell lines and mouse β cells (Velasco and Petersen, 1987; Satin et al., 1989; Kukuljan et al., 1991; Houamed et al., 2010). Smith et al. (1990b) found that the amplitude of the whole cell outward current was not affected by chelation of intracellular Ca^{2+} by adding [EGTA] to pipette solutions, but they observed that a transient component was depressed by blocking I_{CaV}. Furthermore, single-channel recordings demonstrated that this current was activated immediately after the onset of a depolarizing pulse. These findings suggested that the channel might be functionally coupled to Ca^{2+} channels rather than to bulk cytosolic $[Ca^{2+}]$. Similar transient outward currents coupled with I_{CaV} have also been reported in human β cells (Herrington et al., 2005; Braun et al., 2008). Because it is difficult to estimate $[Ca^{2+}]$ near the BK channel molecule, this current was tentatively represented as a V-dependent transient K^+ current based on the above properties (Eqs. S32–S37). The rate constants for activation and inactivation were determined based on the measurement in dissociated mouse β cells at 33.5°C (Houamed et al., 2010). It has been suggested that this current is a major determinant of the action potential amplitude (Henquin, 1990; Braun et al., 2008; Houamed et al., 2010; Jacobson et al., 2010). Thus, the conductance of $I_{KCa(BK)}$ was determined to set an action potential peak from −10 to 0 mV (Eq. S31).

ATP-sensitive K^+ current (I_{KATP}). It has been well established that the open probability of ATP-sensitive K^+ channel changes depending on the intracellular energy status (Cook and Hales, 1984; Rorsman and Trube, 1985), and thereby I_{KATP} modulates membrane excitability and subsequent insulin secretion in β cells (Larsson et al., 1996). Hopkins et al. (1992) suggested that the channel activity is dependent on ADP level over the concentration range of 10–100 μM, rather than on the ATP/ADP ratio (Dunne and Petersen, 1986; Misler et al., 1986). Based on a reaction scheme with two ADP-binding sites (Hopkins et al., 1992), Magnus and Keizer (1998) proposed a detailed model of I_{KATP}. We adopted this model after a minor modification of dissociation constants for ATP and MgADP according to experimental data (Ashcroft and Kakei, 1989; Hopkins et al., 1992).

Rorsman and Trube (1985) found that the input conductance was ~0.05 nS (20 GΩ in the input resistance) at 10 mM [G], but it increased to 1.9 ± 0.1 nS/pF when ATP was omitted from the intracellular solution. Subsequently, Smith et al. (1990a) observed a similar increase of input conductance to 5.1 ± 0.9 nS under 0 mM [G], which was almost completely inhibited by tolbutamide, a selective K_{ATP} channel blocker. Because these data could constrain the maximum conductance of I_{KATP} (G_{KATP}; Eq. S53) in our model, we simulated a corresponding measurement with a voltage-clamp step from −70 to −80 mV. The whole cell input conductance ranged from 0.048 to 0.068 nS during bursting rhythm at 10 mM [G], which was in good agreement with the experimental value

(Rorsman and Trube, 1985). Under zero intracellular ATP, however, the input conductance only increased to 0.9 nS, >90% of which was attributed to K_{ATP} conductance. This value was much smaller than the experimental measurements. However, we failed to improve G_{KATP} of the original model of I_{KATP} (Magnus and Keizer, 1998), and this problem was left for future work.

Ca^{2+}-activated K^+ current ($I_{KCa(SK)}$). In islet preparations, Göpel et al. (1999a) recorded a novel K^+ current component (I_{Kslow}), which was activated with a slow time constant of ~2.3 s during a train of depolarizing pulses and deactivated with a time constant of 6.5 s after the pulses. An analogous current was also recorded in dispersed mouse β cells in several studies (Göpel et al., 1999a; Goforth et al., 2002; Zhang et al., 2005; Düfer et al., 2009). The pharmacological and gene knockout studies have suggested that small-conductance K_{Ca} (SK) channels might contribute substantially to I_{Kslow} (Zhang et al., 2005; Düfer et al., 2009). Supporting this view, isoforms of SK −1 to −4 were found to be expressed at the level of mRNA and protein in mouse β cells (Tamarina et al., 2003; Düfer et al., 2009). Interestingly, Kanno et al. (2002) ascribed ~50% of the experimental I_{Kslow} to I_{KATP}. Thus, we implemented the SK channel current as $I_{KCa(SK)}$ in our new model separately from I_{KATP}. The Ca^{2+} dependency for activation of $I_{KCa(SK)}$ was adopted from Hirschberg et al. (1998) (Eq. S38). It seems that the activation by Ca^{2+} of SK current is almost instantaneous, but slow changes in $[Ca^{2+}]_i$ and/or the contaminated I_{KATP} component might result in the slow time course of I_{Kslow} in experimental recordings.

Background nonselective cation current (I_{bNSC}). Henquin and Meissner (1984a) showed that the resting membrane potential of β cells is less negative than the K^+ equilibrium potential. They attributed this depolarizing effect to a basal membrane Na^+ conductance (see also Ashcroft and Rorsman, 1989). It is now well established that this background Na^+ conductance includes several types of currents. Nevertheless, a background cation current is still required to establish the resting potential, especially when I_{CRAN} is largely inactivated. Thus, we added such a current, I_{bNSC}, of an unspecified nature. Note that many previous β-cell models also included a background current component (Chay and Keizer, 1983; Chay, 1996; Magnus and Keizer, 1998; Meyer-Hermann, 2007; Fridlyand et al., 2009). I_{bNSC} in this model is permeable to Na^+ and K^+ with a reversal potential at approximately −20 mV (Eqs. S40–S42). The conductance was adjusted to give both the resting membrane potential and input impedance consistent with experimental measurements at a low [G] (Rorsman et al., 1986; Rorsman and Trube, 1986).

Plasma membrane Ca^{2+} pump (PMCA) and Na^+/Ca^{2+} exchange (NCX) currents (I_{PMCA}, I_{NaCa}). Ca^{2+} influx through I_{CaV} is balanced with Ca^{2+} efflux via I_{PMCA} (PMCA1, 2, and 3) and I_{NaCa} (NCX1) (Váradi et al., 1995; Herchuelz et al., 2007). PMCA has one Ca^{2+}-binding site and 1:1 Ca^{2+}/ATP stoichiometry (Brini and Carafoli, 2009). PMCA2 has an apparent Hill coefficient of ~2 (Caride et al., 2001) and the half-maximal concentration of ~0.1 μM $[Ca^{2+}]_i$ in the presence of calmodulin (Enyedi et al., 1991; Elwess et al., 1997). Based on these findings, I_{PMCA} is expressed by a Hill equation (Eq. S95). In addition, it is known that PMCA exchanges one intracellular Ca^{2+} for one extracellular H^+ (Hao et al., 1994), and we assumed that the excess H^+ was instantaneously removed by Na^+/H^+ exchange. Because Na^+/H^+ exchange was not included in the present model, the resultant Na^+ influx by the functional coupling of PMCA and Na^+/H^+ exchange was directly included in calculating $d[Na^+]_i/dt$ (Eq. S3).

The description of I_{NaCa} was adopted from a cardiac myocyte model (Takeuchi et al., 2006), which describes time-dependent transitions between different functional states of the NCX molecule (Eqs. S75–S94). The slope conductance of I_{NaCa} near the reversal potential was 25.5 pS pF^{-1} at 14 μM $[Ca^{2+}]_i$ and 30 mM $[Na^+]_i$ in the present model, which is about half of the experimental value (53 pS pF^{-1}) (Gall et al., 1999). This difference seems to fall within the range of experimental variations because of the limited intracellular perfusion with pipette solutions through the ruptured patch.

NaK current (I_{NaK}). The I_{NaK} model was adopted from Oka et al. (2010), in which the turnover rate was precisely described in terms of V_m, intracellular, and extracellular compositions of Na^+ and K^+, and the free energy of ATP hydrolysis (ΔG_{ATP}) based on thermodynamics (Eqs. S54–S74). Although this model was developed with reference to experimental measurements in cardiac myocytes, we assumed for convenience that the basic characteristics of the pump activity would be common in β cells. In addition, the inhibition of the pump activity by glucose via intracellular signaling (Owada et al., 1999) was implemented (F_{glc}; Eq. S55). The amplitude factor of I_{NaK} (P_{NaK}) was determined to satisfy Na^+ homeostasis in both quiescent and bursting activities. Finally, the K^+ balance between efflux through K^+ channels and the active influx via NaK was calculated, rather than fixing $[K^+]_i$ as in the original FP model.

Modeling intracellular Ca^{2+} dynamics

A precise description of ER Ca^{2+} dynamics is critical for modeling β-cell function. Uptake of Ca^{2+} into the ER is mediated by ER Ca^{2+} ATPase (SERCA), and approximately equal amounts of SERCA 2b and 3 are expressed in pancreatic islets (Váradi et al., 1996). The apparent affinity for cytosolic Ca^{2+} was determined with a half-activation concentration ($K_{1/2}$) of 0.27 and 1.1 μM, and a Hill coefficient (n^H) of 1.7 and 1.8 for SERCA 2b and 3, respectively (Lytton et al., 1992). The SERCA activity in the present study was represented with a Hill equation of $K_{1/2} = 0.5$ μM and $n^H = 2$, compromised for the whole cell simulation (Eq. S96). Ca^{2+} release from ER is a critical determinant for reconstructing the slow decay phase of $[Ca^{2+}]_i$ observed after action potential burst. Although an application of IP_3 facilitates Ca^{2+} release (Tengholm et al., 2001), the slow Ca^{2+} decay during the interburst did not seem to be triggered by IP_3-, depolarization-, nor Ca^{2+}-induced Ca^{2+} release (Gilon et al., 1999). Therefore, ER Ca^{2+} release (J_{rel}) was described as a passive flux down a concentration gradient in this study (Eq. S97).

ER volume (vol_{ER}), maximum velocity of SERCA (P_{SERCA}; Eq. S96), nor the permeability of the Ca^{2+} release channel (P_{rel}; Eq. S97) has been fully measured to provide definite values of these parameters. Thus, they were adjusted based on the following experimental findings. (a) The physiological level of $[Ca^{2+}]_i$ hardly exceeds 0.5 μM during glucose stimulation (Rorsman et al., 1984). (b) The resting $[Ca^{2+}]_i$ is 60–100 nM (Rorsman et al., 1992; Chow et al., 1995). (c) Onset and offset time courses of Ca^{2+} transient were recorded, which were evoked by the action potential burst, a voltage-clamp pulse, or K^+-induced depolarization (Gall et al., 1999; Gilon et al., 1999). (d) Direct measurement of $[Ca^{2+}]_{ER}$ using a low affinity Ca^{2+} fluorescent dye revealed that $[Ca^{2+}]_{ER}$ is maximally increased up to ~200 μM by Ca^{2+} uptake through SERCA in the absence of IP_3 (Tengholm et al., 2001). It was consistent with $[Ca^{2+}]_{ER}$ of 60–200 μM suggested previously (Tse et al., 1994). (e) At 12 mM [G], Ca^{2+}-stimulated ATPase activity of SERCA was comparable to that of PMCA in β cells (Roe et al., 1994). In the present β-cell model, the ratio of ATP consumption by SERCA and PMCA was approximately 1:1 at 12 mM [G], ranging from 1:3 in a quiescent state at 6 mM [G] to 4:3 during continuous firing at 20 mM [G].

Modeling energy metabolism

Fridlyand et al. (2005) elaborated a set of equations for ATP production through glycolysis and oxidative phosphorylation, and for ATP consumption based on a wide range of biochemical studies. We used their model with a few modifications as follows. First, we changed the glucose dependency of glycolysis (f_{glc}) (Eq. S100) to reproduce the experimental finding that the burst duration is prolonged with increasing [G] in β cells. Our revision might be appropriate because f_{glc} reflects the [G] dependency of all the reaction steps including glycolysis and TCA cycle in our model. Note that the original values in the FP model were determined under the assumption that glucose phosphorylation by glucokinase was the only limiting step in glycolysis. Second, we calculated ATP production via β oxidation of fatty acid ($J_{\beta,ox}$; Eq. S99), in addition to glycolysis (J_{glc}; Eq. S98). This modification prevented the system from a metabolic collapse at a low [G] (<2 mM), which actually occurred in the FP model. Third, in the production of reduced metabolic compounds (Re), we took account of the total amount of pyridine nucleotides ([Re_{tot}]) by adding a term of ([Re_{tot}] − [Re]) in J_{glc} and $J_{\beta,ox}$ (Eqs. S98 and S99). This term was crucial to avoid an unlimited increase of [Re] at a high [G] (>15 mM), observed in the FP model. Under the assumption that most Re consists of NADH in the mitochondria, [Re_{tot}] of 10 mM was used (Cortassa et al., 2003). The consumption of [Re] by oxidative phosphorylation was calculated using a stoichiometry of 2.5 between ATP and NADH, and with a volume ratio (2.5) between the cytosol and mitochondria (Eq. S102).

Lead potential (V_L) analysis

To clarify the ionic mechanisms underlying burst–interburst rhythm in our new β-cell model, we applied the V_L analysis developed by Cha et al. (2009). The method quantifies the contributions of individual membrane currents to changes in V_m by calculating an equilibrium potential at each moment (V_L) using the time-varying conductance (G_X), reversal potential (E_X), and V-independent transporter current (I_Y),

$$V_L = \frac{\sum_X G_X E_X - \sum_Y I_Y}{\sum_X G_X}. \quad (1)$$

Also refer to Eq. S108. V_L always moves in advance of V_m, and its time derivative (dV_L/dt) drives the automatic change of V_m. The relative contribution (r_c) of a current component of interest (i) is defined by a relative change in dV_L/dt when the time-dependent change of i is selectively fixed. The total sum of r_c for all components equals unity at each time point, and is used to validate the calculations,

$$r_{c,i} = \frac{\frac{dV_L}{dt} - \frac{dV_{L\_Fix,i}}{dt}}{\frac{dV_L}{dt}} \text{ and } \sum_i r_{c,i} = 1. \quad (2)$$

This method has been verified in various cardiac cell models (Cha et al., 2009; Himeno et al., 2011). In the present study, the contribution c (mV s^{-1}) was used, instead of r_c. c was newly defined by the following equation:

$$c_i = \frac{dV_L}{dt} - \frac{dV_{L\_Fix,i}}{dt} \text{ and } \sum_i c_i = \frac{dV_L}{dt}. \quad (3)$$

c with a positive sign indicates that the corresponding component contributes to membrane depolarization, and vice versa.

Among the three electrogenic ion transporters, V-independent I_{PMCA} was treated as a current source (Eq. S108). I_{NaK} and I_{NaCa} were expressed with Eqs. 4 and 5, where G_{NaK} and G_{NaCa} are the slopes of tangential lines fitted to the instantaneous I-V relation at each moment, and E_{x_NaK} and E_{x_NaCa}, the intersections of the tangential lines with the x axis:

$$I_{NaK} = G_{NaK}(V_m - E_{x\_NaK}) \quad (4)$$

$$I_{NaCa} = G_{NaCa}(V_m - E_{x\_NaCa}). \quad (5)$$

The contribution of I_{NaK} or I_{NaCa} in Fig. 5 was a summation of c evaluated by fixing G_{NaK} and E_{x_NaK}, or G_{NaCa} and E_{x_NaCa}, respectively. Because G_{NaK} and E_{x_NaK} are functions of $[Na^+]_i$, $[K^+]_i$, [ATP] or [MgADP], and V_m, the contribution of each concentration change was also evaluated in the bottom panels of Fig. 5.

Online supplemental material

Equations, parameters, and the definition of symbols of the β-cell model are provided in the supplemental material. Table S1 lists the initial values of the 18 variables in this model. Figs. S1 and S2 show reconstructions of I_{CaV} and I_{KDr} in voltage-clamp experiments, respectively. Fig. S3 shows the effect of thapsigargin on the Ca^{2+} transients induced by applying high K^+ pulses to the model. Fig. S4 is V_L diagram of the FP model for comparison to our model (Fig. 5). The supplemental material is available at http://www.jgp.org/cgi/content/full/jgp.201110611/DC1.

RESULTS

Electrical activity and intracellular concentrations of ions and metabolites in pancreatic β cells

Burst of action potentials evoked by various glucose concentrations. Fig. 2 shows the time-dependent changes in V_m, [ATP], [MgADP], $[Na^+]_i$, and $[Ca^{2+}]_i$ evoked by different [G] in the new β-cell model. At [G] < 6 mM, the membrane was quiescent, and the concentrations of intracellular ions and metabolites remained at various steady-state levels depending on [G]. The resting potential decreased from −70 mV at 0 mM [G] (not depicted) to −58 mV at 6 mM [G], accompanied by an increase in the input impedance from 4 to 15 GΩ. This input impedance is comparable to experimental measurements of 3–30 GΩ (Rorsman and Trube, 1986), 1–10 GΩ (Rorsman et al., 1986), or 3 GΩ (Smith et al., 1990a). In the simulation, the increase in input impedance largely resulted from the progressive closure of I_{KATP} channels. At 7 mM [G], a typical burst of action potentials appeared. The burst duration was elongated as [G] increased, and finally the burst was transformed to a continuous firing at [G] > 19 mM (Ashcroft et al., 1984; Henquin and Meissner, 1984b). The interburst phase is also elongated at a higher [G] in the present study because more time was required to recover from ion accumulation during the preceding burst period of longer duration. This simulation result is in agreement with the experimental data from mouse islets showing longer burst and interburst periods at a higher [G] (Antunes et al., 2000). Our model, however, failed to reconstruct gradual shortening of the interburst period with [G] (Meissner and Schmelz, 1974).

The action potential in the model is in good agreement with the representative burst activity recorded in a single β cell in the presence of 2.6 mM $[Ca^{2+}]_o$ and 10 mM [G] at 31°C (see Fig. 1 B in Smith et al., 1990a). The maximum rate of rise was 2–3 V s^{-1} in the model, comparable to 3.2 V s^{-1} (Rorsman and Trube, 1986) or 3.5 V s^{-1} (Dean et al., 1975). The peak potential was about −4 mV in the model versus −8.3 mV experimentally (Smith et al., 1990a), the plateau potential was about −50 versus −53.7 mV, and the maximum negative potential during the interburst period was about −68 versus −76.4 mV. The maintenance of the plateau potential was mainly attributable to I_{CaV} conductance remaining at the end of the action potentials. It was supported by a simulation showing that the burst was interrupted if I_{CaV} was instantaneously deactivated by applying a brief hyperpolarizing voltage pulse (not depicted). The Ca^{2+}-activated inward currents, I_{TRPM} and I_{NaCa}, also contributed to the maintenance of the plateau potential.

Slow fluctuations in [ATP], [MgADP], $[Na^+]_i$, and $[Ca^{2+}]_i$ during burst–interburst rhythm. In our model, [ATP] and [MgADP] changed in synchrony with electrical events at [G] > 7 mM (Fig. 2, second row). That is, [MgADP] increased at the expense of ATP during the burst and in turn decreased during the subsequent quiescent period when the cell was relieved from the extra Ca^{2+}-dependent ATP consumption. These typical responses were observed at 8 mM [G]. At 12 or 16 mM [G], however, the ATP consumption was compensated for to a greater extent by increased ATP production. Thus, [MgADP] increased much slower during the burst, and its maximum level at the end of burst was lower in spite of the elongated burst duration. On the other hand, the fluctuation in $[Na^+]_i$ was enlarged with an increase in burst duration, and finally $[Na^+]_i$ remained elevated at [G] > 19 mM (Fig. 2). Accumulation of $[Na^+]_i$ was mostly a result of Na^+ influx through NCX, which compensated for the large Ca^{2+} influx through I_{CaV}. Based on the opposite changes in the fluctuations of [ATP] and $[Na^+]_i$ by increasing [G], our β-cell model predicted that the activation of I_{NaK} by the accumulation of $[Na^+]_i$ might take over the role of I_{KATP} in terminating the burst at a higher [G].

Fluctuation in $[Ca^{2+}]_i$ during the burst–interburst rhythm also has profound effects on the electrical activity. As demonstrated in Fig. 2, $[Ca^{2+}]_i$ jumped from a resting level of ~100 to ~400 nM at the onset of the burst, and then the plateau level of the oscillation (fast Ca^{2+} ripple) slowly decreased during the burst, because of the slow inactivation of I_{CaV}. At [G] > 12 mM, a brief oscillation in the plateau level of the Ca^{2+} ripple preceded the final termination of the burst, which has not been described by experimental studies. We found that this oscillation was sensitive to the amplitude of $I_{KCa(SK)}$ but failed to clarify the underlying mechanisms in the present study. After cessation of the burst, a slow decay

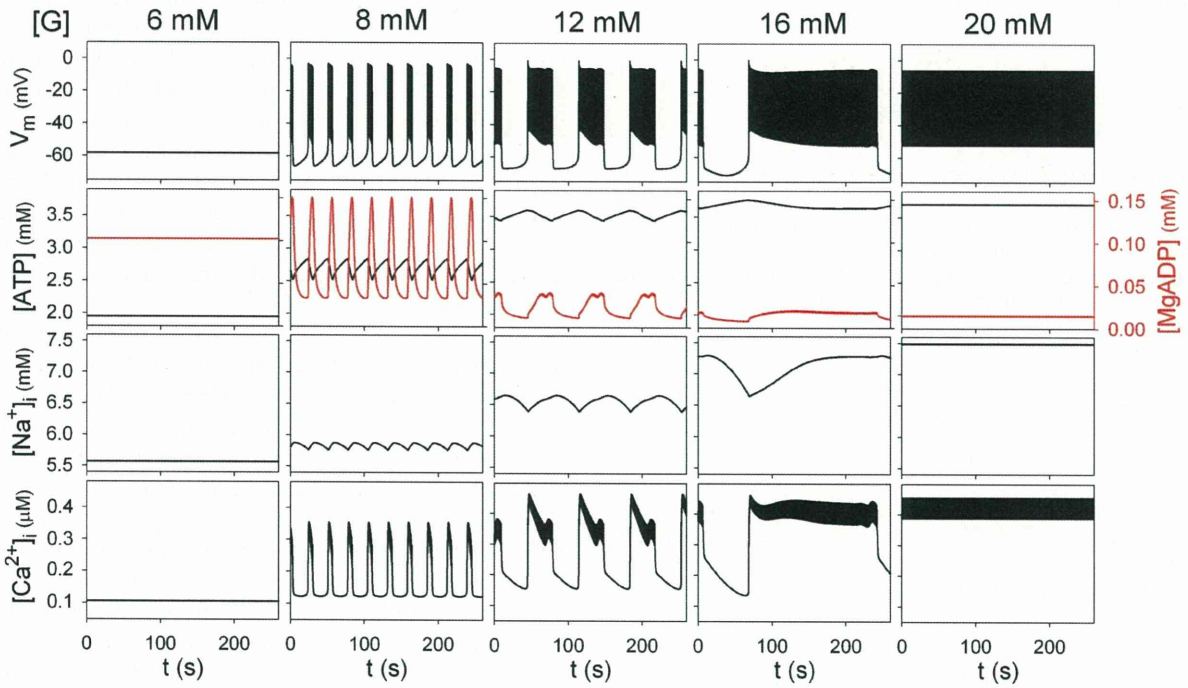

Figure 2. Activities of the β-cell model at various [G]. Each row indicates steady cyclic changes in V_m, [ATP] (black), [MgADP] (red), $[Na^+]_i$, and $[Ca^{2+}]_i$ in the presence of 8, 12, and 16 mM [G], or a quiescent state at 6 mM [G] and continuous firing of the action potentials at 20 mM [G]. All records were obtained with initial values in Table S1 after the rhythm of the cyclic events became stable after switching [G].

phase (or Ca^{2+} tail) was observed at 12 and 16 mM [G], but hardly at 8 mM [G]. This Ca^{2+} tail is caused by release of Ca^{2+} from the ER, which has accumulated during the preceding burst. The increase in the Ca^{2+} fluctuation at a higher [G] has complex influences on membrane ion channels or transporters, that is, activation of outward-going I_{PMCA} or $I_{KCa(SK)}$, as well as inward-going I_{NaCa} or I_{TRPM}. The overall effects of $[Ca^{2+}]_i$ will be evaluated mathematically later.

Role of ER Ca^{2+} dynamics in glucose-induced burst–interburst rhythm

Ca^{2+} dynamics in the new β-cell model were validated before we analyzed the ionic mechanisms. In control conditions, a regular burst–interburst rhythm and the accompanying Ca^{2+} transients were generated with a cycle length of ~40 s at 11 mM [G] (Fig. 3, the left half). At the onset of a burst, most Ca^{2+} influx through I_{CaV} was instantaneously captured by cytosolic Ca^{2+}-binding proteins (f_i in Eq. S5). Then, during the initial 1 s of the burst, the Ca^{2+} influx was compensated for by the ER (J_{SERCA}-J_{rel}; 44%), PMCA (26%), and NCX (34%) (Fig. 3, bottom), which was in good agreement with experimental results (Gall et al., 1999). As the burst progressed, Ca^{2+} gradually accumulated in the ER, and thus the ER Ca^{2+}-buffering capacity became less effective because of an increase in Ca^{2+} release from the ER. Importantly, 97% of the Ca^{2+} accumulated during the whole burst was taken up by the ER, and only 3% remained in the cytosol. After cessation of the burst, the accumulated Ca^{2+} in the ER was slowly released into the cytosol (Fig. 3, bottom), which is a main contributor of the long-lasting Ca^{2+} tail. This simulation result is in line with experimental responses (Gilon et al., 1999).

For further examination of the relevance of the Ca^{2+} dynamics in the model, the effects of blocking SERCA by thapsigargin were simulated. In the right half of Fig. 3 indicated by a gray horizontal bar, the activity of SERCA was reduced to 20% of the control. As a result, the Ca^{2+}-buffering capacity of ER decreased, and in the steady state, the amplitude of Ca^{2+} oscillation was increased by nearly two times. In addition, the Ca^{2+} tail disappeared from the interburst period and the electrical rhythm became about two times faster through the shortening of both interburst and burst periods. These findings are in good agreement with several experimental recordings (Miura et al., 1997; Gilon et al., 1999; Fridlyand et al., 2003) and previous simulation results (Fridlyand et al., 2003; Bertram and Sherman, 2004). The rate of depolarization during the interburst was accelerated by the activation of inward I_{SOC} as a result of ER depletion. The burst duration was also reduced because the opening of I_{KATP} was accelerated by the enhanced Ca^{2+}-dependent ATP consumption. Increased outward $I_{KCa(SK)}$ or I_{PMCA} by the amplified Ca^{2+} transient might also help the early termination of the burst, whereas inward I_{NaCa} and I_{TRPM} have the opposite effects.

We also simulated Ca^{2+} transients induced by applying 45 mM of K^+ solution (Fig. S3). The Ca^{2+} tail observed after the high K^+ pulse was well reconstructed (Gilon et al., 1999). The simulation predicted that $[Ca^{2+}]_{ER}$ was accumulated up to ~60 μM via I_{CaV} activated through high K^+-induced depolarization (approximately −25 mV). In the presence of thapsigargin, the amplitude of Ca^{2+} transients was increased with a large initial peak, and the slow Ca^{2+} tail disappeared. The slow inactivation of I_{CaV} caused the marked decrease in $[Ca^{2+}]_i$ during the initial 10 s of the pulse, as well as the temporal depression after washing out the high K^+ solution.

Ionic mechanisms underlying the electrical activity of β cells

Current profile during the burst and interburst periods. The findings in Fig. 2 suggested that the burst rhythm is determined by the balance among current components

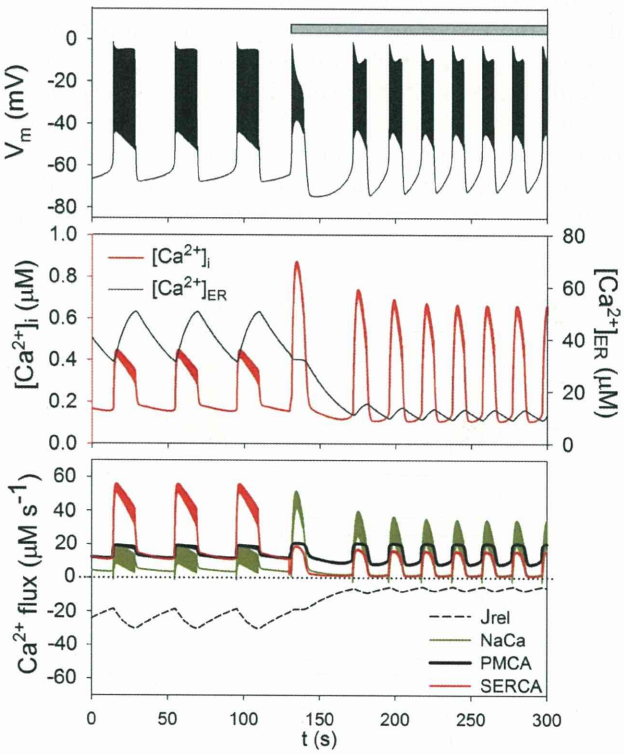

Figure 3. Dynamics underlying spontaneous Ca^{2+} oscillations before and after inhibition of SERCA. Time-dependent changes in V_m (top), and $[Ca^{2+}]_i$ and $[Ca^{2+}]_{ER}$ (middle), and Ca^{2+} fluxes through J_{rel}, J_{SERCA}, I_{NaCa}, and I_{PMCA} (bottom) at 11 mM [G] are illustrated with different colors, as indicated in each panel. The scale of $[Ca^{2+}]_{ER}$ is represented on the right y axis (middle), and the zero flux level is indicated by a dotted line (bottom). From 130 s (gray horizontal bar), P_{SERCA} was reduced to 20% of its control value (from 0.096 to 0.0192 amole ms^{-1}) to simulate the blocking effect of SERCA by thapsigargin. The net Ca^{2+} flux through the ER was calculated by subtracting J_{rel} from J_{SERCA}.

that are modulated by slow changes in [ATP] and [MgADP], as well as those in $[Na^+]_i$ and $[Ca^{2+}]_i$. We measured the amplitudes of all these currents, including I_{KATP}, I_{NaK}, I_{NaCa}, I_{PMCA}, I_{TRPM}, and $I_{KCa(SK)}$, at 8 and 16 mM [G], in addition to V-dependent I_{CaV} and I_{KDr} (Fig. 4). During the burst period, the current levels were measured at the most negative potential between successive action potentials. The plateau potential gradually shifted negative toward the threshold for the full repolarization of the burst termination. At both [G], I_{KDr} was of minimum size because of almost complete deactivation at the end of individual action potentials, and its contribution to changing the plateau potential seemed to be negligible. In contrast, I_{CaV} had the largest amplitude, suggesting that it is the major current maintaining the plateau potential or driving the interburst depolarization to trigger the subsequent action potential burst. I_{KATP} provided a sizable outward current during the interburst at 8 mM [G] but was much decreased at 16 mM [G]. In contrast, outward I_{NaK} and $I_{KCa(SK)}$, and inward I_{NaCa} and I_{TRPM}, were substantially increased at 16 mM [G] by the accumulation of $[Na^+]_i$ and $[Ca^{2+}]_i$ during the prolonged burst period. The amplitude of I_{SOC} was negligibly small throughout the records in Fig. 4 at both 8 and 16 mM [G] (not depicted). These current profiles, however, only give clues as to the contribution of individual currents underlying the generation of electrical bursting activity. A quantitative understanding of the ionic mechanisms requires further mathematical analysis, such as V_L analysis in the next section or bifurcation analysis as described in our companion paper (see Cha et al. in this issue).

V_L analysis of interburst ionic mechanisms. To measure the contribution of each current component to automatic change in V_m, V_L analysis was applied to the simulation results (Eqs. 1, 3, and S108). The magnitudes of the contribution (c in mV s^{-1}; see Materials and methods) of individual ion channels and transporters were calculated over the interburst period, as indicated with horizontal gray bars in Fig. 4 (A and B). c was plotted in a cumulative manner at 8 and 16 mM [G] (Fig. 5, middle panels).

At 8 mM [G], V-dependent activation of I_{CaV} (d_{CaV}), albeit a tiny change from 0.03 to 0.05, provided the largest positive contribution during the entire course of slow depolarization (Fig. 5 A). In contrast, the contribution of ultraslow inactivation of I_{CaV} (f_{us}) was trivial. I_{KATP}, an outward current, also provided a positive contribution to the depolarization ($c \sim 0.1$–0.2 mV s^{-1}) because its open probability was gradually reduced by both increasing [ATP] and decreasing [MgADP]. In the late phase, the contribution of I_{KATP} became smaller by gradual equilibration of [ATP] and [MgADP]. The positive contribution of inward I_{NaCa} ($c < 0.1$ mV s^{-1}) was mainly attributable to increased turnover rate by the gradual decrease of $[Na^+]_i$ after cessation of the burst. I_{NaK}, $I_{KCa(BK)}$, and I_{TRPM} hindered the slow depolarization, as

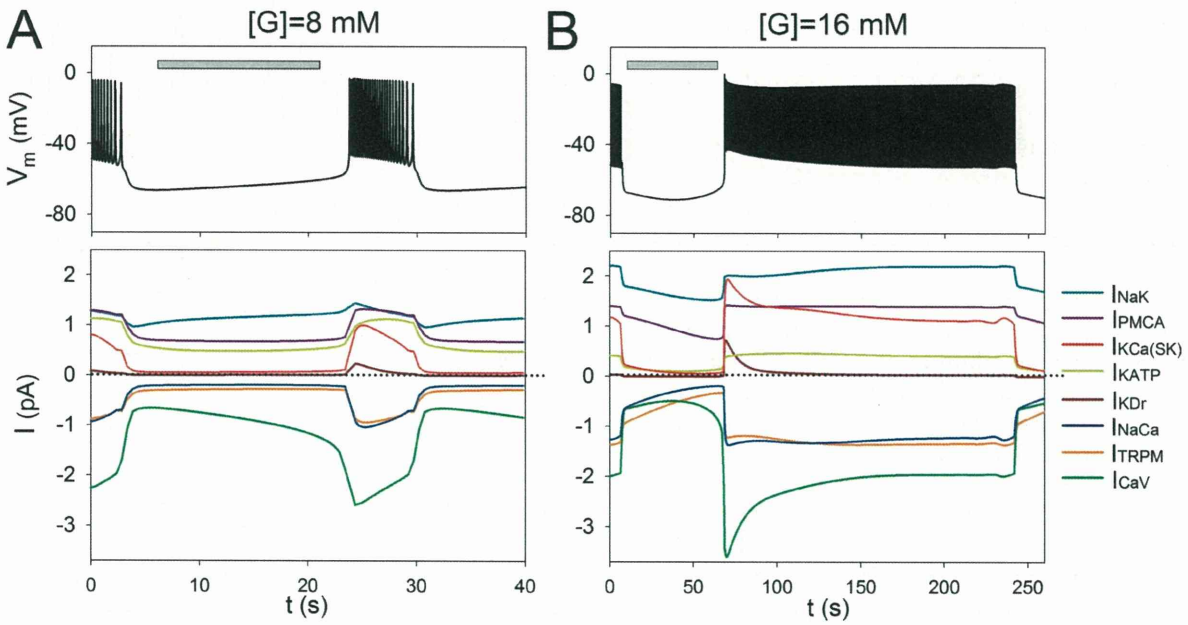

Figure 4. Ionic currents during burst and interburst activity at 8 mM [G] (A) and 16 mM [G] (B). Top panels show V_m and bottom panels show individual ionic currents, with the different colors as indicated on the right. The amplitudes of individual currents were measured at the plateau potential (the most negative potential between successive action potentials) during the burst period. Note that different time scales are used in A and B. The zero current level is indicated by dotted lines. Gray bars indicate the interburst period, where the V_L analysis was applied in Fig. 5.

represented by their negative contributions (less than -0.2 mV s^{-1}).

At 16 mM [G], the ionic mechanisms changed markedly (Fig. 5 B). The contribution of I_{KATP} almost disappeared from the V_L diagram, but the contribution of Ca^{2+}-dependent currents (I_{PMCA}, I_{NaCa}, and I_{TRPM}) noticeably increased in compared with those at 8 mM [G]. The V_m change showed two phases during the interburst period: early hyperpolarization and late depolarization. During the early phase, the hyperpolarization was mainly attributed to decreases in inward I_{NaCa} and I_{TRPM} as a result of the slow decay of $[Ca^{2+}]_i$. The sum of these hyperpolarizing effects was larger than the depolarizing effect caused by the decrease in outward I_{PMCA}. In the late phase, the decay rate of $[Ca^{2+}]_i$ slowed down, the contribution of I_{NaCa} was reversed by the decrease in $[Na^+]_i$, and the negative contribution of I_{TRPM} was also reduced. Furthermore, the decrease in $[Na^+]_i$ gradually reduced outward I_{NaK} and contributed to depolarization. As a consequence, the membrane started to depolarize at the late phase.

Comparison of the V_L diagrams in Fig. 5 (A and B) reveals that a metabolic-dependent mechanism (I_{KATP}) at a lower [G] was replaced by an ion-dependent mechanism (I_{PMCA}, I_{NaCa}, and I_{TRPM}) at a higher [G] in generating the burst–interburst rhythm. This replacement of mechanism was further exemplified by separating the contribution of I_{NaK} into metabolism- and ion-dependent mechanisms (Fig. 5, bottom panels). At 8 mM [G], a negative contribution of I_{NaK} was caused by rapid recovery of the ATP/MgADP composition, whereas at 16 mM [G], the metabolic effects almost disappeared, and the decrease in $[Na^+]_i$ dominated the time course of c of I_{NaK}.

V_L analysis of repetitive action potentials. The result of V_L analysis is presented in Fig. 6 for two successive action potentials during the burst. The V_L (Fig. 6, red line) leads the time-dependent change in V_m (black line) in advance and intersects the V_m curve when dV_m/dt (or I_{tot}) equals zero. The V_L diagram (Fig. 6, bottom) indicates that the time course of the action potential is largely determined by I_{CaV}. In the rising phase of the spontaneous action potential, the progressive V-dependent activation of I_{CaV} plays the major role; likewise, the V-dependent deactivation of I_{CaV} is mainly responsible for repolarization. The activation of $I_{KCa(BK)}$ partially counteracts I_{CaV} to reduce the maximum rate of rise or decay of the action potential. Surprisingly, the delayed activation of outward I_{KDr} provided a negative contribution only at the beginning of the repolarizing phase, but then reversed its contribution to retard the repolarizing influence of I_{CaV}. This retarding effect of I_{KDr} is a result of V-dependent removal of activation (p_{KDr}). The contributions of the other substrate-dependent currents, I_{KATP}, I_{PMCA}, I_{NaCa}, I_{TRPM}, and I_{NaK}, are barely

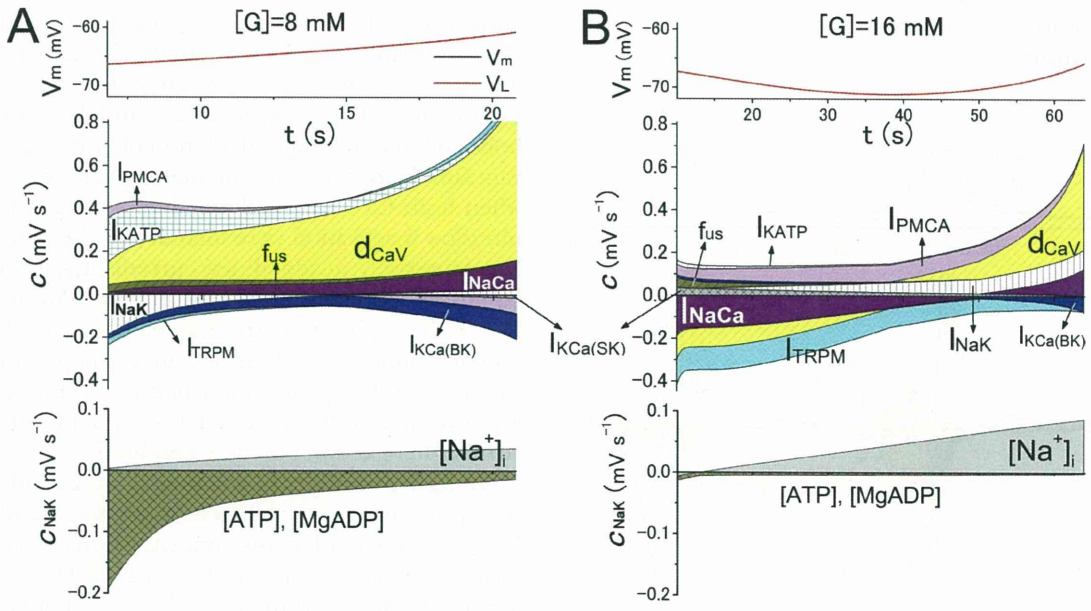

Figure 5. V_L diagrams show the contribution of major currents during the interburst period at 8 mM [G] (A) and 16 mM [G] (B). (Top) Time-dependent changes in V_L (red) and V_m (black). The V_m trace is overlapped by V_L. (Middle) Time-dependent changes in the contribution (c) of individual currents indicated with different colors. A positive c indicates that the time-dependent change in the corresponding current contributes to depolarization (in mV s^{-1}), and vice versa. The contribution of I_{CaV} was divided into c of d_{CaV} and c of f_{us}. The rest for I_{CaV} was negligibly small (not depicted). (Bottom) Separation of the contribution of I_{NaK} into [ATP]- and [MgADP]-dependent components (dark yellow) and $[Na^+]_i$-dependent component (gray). Effects of other factors on I_{NaK}, such as time-dependent changes in $[K^+]_i$ or V_m, were negligibly small (not depicted). The time scales refer to those for the gray bars in Fig. 4 (A and B).

visible because the concentrations of ions or metabolites changed minimally over the time span of an action potential.

An extra effect of [G] on the bursting activity through direct inhibition of NaK

Owada et al. (1999) demonstrated that applying glucose to β cells inhibited Na^+/K^+ ATPase in a dose-dependent and reversible manner via a distinct signal transduction pathway. Because this inhibition was of considerable magnitude (up to 55%), they suggested that the inhibition of I_{NaK} might promote insulin secretion at a high [G]. We tested this hypothesis by switching on the inhibitory action of glucose on I_{NaK} (F_{glc}; Eq. S55) after a steady rhythm was established (Fig. 7). Immediately after I_{NaK} was reduced by introducing the glucose inhibition (Fig. 7, gray bar), an action potential burst of longer duration was evoked accompanied by a larger Ca^{2+} transient, in agreement with the experimental observations using an NaK blocker (Bozem and Henquin, 1988). Contrary to the expectation of Owada et al. (1999), the burst interval returned to control at the next burst and remained constant. The amplitude of I_{NaK} was almost restored because $[Na^+]_i$ gradually increased until I_{NaK} exactly matched the Na^+ influx. The basal level of $[Ca^{2+}]_i$ was initially increased by the intervention but slowly recovered over the next 100 s. Similar results were simulated at 12 mM [G]. The simulation suggests that the partial inhibition of I_{NaK} by glucose might increase insulin secretion at 8 mM [G], but the effect is only transitory.

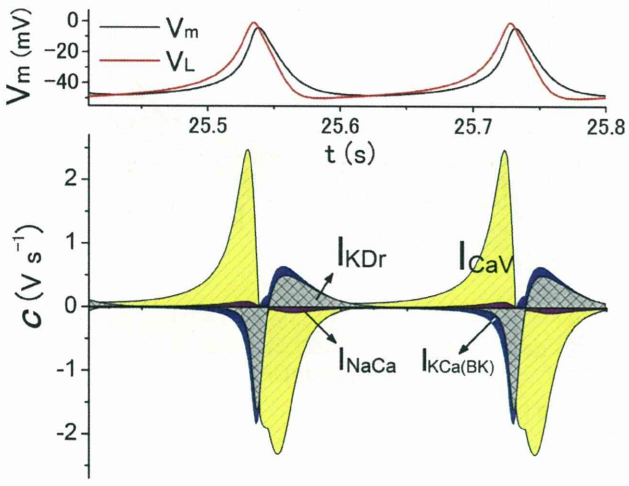

Figure 6. V_L diagram for two successive action potentials within the burst at 8 mM [G]. (Top) Time-dependent changes of V_L (red) and V_m (black). Note that V_L always changes in advance of V_m. (Bottom) Time-dependent changes in contributions (c) of I_{CaV}, I_{KDr}, $I_{KCa(BK)}$, and I_{NaCa}. The c of other currents was also plotted in the diagram but is barely visible because of its minor contributions. The time scale on the x axis refers to that in Fig. 4 A.

DISCUSSION

By integrating a broad range of electrophysiological findings into a mathematical model, the response of pancreatic β cells to extracellular glucose was well reconstructed, and the underlying mechanisms were elucidated in a comprehensive manner. The new β-cell model showed a series of responses to varying [G], that is, the intermittent burst of action potentials accompanied by Ca^{2+} transients at [G] > 7 mM, the elongation of the burst duration with increasing [G], and the continuous firing of action potentials at [G] > 19 mM. V_L analysis of the model successfully quantified contributions of ion channels and transporters to the slow interburst depolarization. It was concluded that alternating burst and interburst events at the physiological range of [G] is regulated mainly by I_{KATP} channels, which transduce signals from varying [ATP] or [MgADP] to membrane excitability. The novel prediction is that the role of I_{KATP} is taken over by electrogenic ion transporters, such as I_{NaCa}, I_{NaK}, I_{PMCA}, and a Ca^{2+}-activated ion channel, I_{TRPM}, at a higher [G].

Comparison with the FP model

To our knowledge, the β-cell model developed by Fridlyand et al. (2003, 2005) provided the first description of individual channels and transporters on a plasma membrane at a molecular level. Our model is based on the structure of this FP model to couple membrane excitation with energy metabolism. We revised most of the ionic current components with reference to more extensive electrophysiological findings. In the FP model, a high K^+ external solution induces continuous Ca^{2+} influx through I_{CaV} (about −30 to −50 pA) and eventually causes a metabolic collapse by a rapid depletion of cytosolic ATP. Relevant simulations to experimental findings were obtained when both Ca^{2+}-mediated inactivation and V-dependent ultraslow inactivation were included in the new model of I_{CaV}. Moreover, we added new currents, I_{TRPM} and $I_{KCa(BK)}$, based on recent experimental findings. We found that I_{TRPM} is an important current to maintain the plateau potential around −50 mV during an action potential burst, whereas a full repolarization between action potentials was observed in the FP model. $I_{KCa(BK)}$ is important in the regulation of action potential amplitude.

For self-consistency of the model, we included all ion transports across the cell membrane in calculating both V_m and intracellular ion concentrations, according to charge conservation law (see Cha et al., 2011). (a) We took account of the H^+ influx via Ca^{2+}/H^+ exchange through PMCA. This H^+ flux was assumed to be completely converted to equivalent Na^+ flux by a fast Na^+/H^+ exchange (see Materials and methods). (b) $[K^+]_i$ was not fixed in our model, but the time-dependent change was calculated by K^+ fluxes through NaK and ion channels. These modifications were prerequisite for examining